



The TESS-Keck Survey. II. An Ultra-short-period Rocky Planet and Its Siblings Transiting the Galactic Thick-disk Star TOI-561

Lauren M. Weiss¹ , Fei Dai² , Daniel Huber¹ , John M. Brewer³ , Karen A. Collins⁴ , David R. Ciardi⁵ , Elisabeth C. Matthews⁶ , Carl Ziegler⁷ , Steve B. Howell⁸ , Natalie M. Batalha⁹ , Ian J. M. Crossfield¹⁰ , Courtney Dressing¹¹ , Benjamin Fulton¹² , Andrew W. Howard¹³ , Howard Isaacson^{14,15} , Stephen R. Kane¹⁶ , Erik A. Petigura¹⁷ , Paul Robertson¹⁸ , Arpita Roy¹³ , Ryan A. Rubenzahl^{13,51} , Joseph D. Twicken^{8,19} , Zachary R. Clayton¹ , Keivan G. Stassun²⁰ , Mason G. MacDougall¹⁷ , Ashley Chontos^{1,51} , Steven Giacalone²¹ , Paul A. Dalba^{16,52} , Teo Mocnik²² , Michelle L. Hill¹⁶ , Corey Beard¹⁸ , Joseph M. Akana Murphy^{23,51} , Lee J. Rosenthal¹³ , Aida Behmard^{24,51} , Judah Van Zandt¹⁷ , Jack Lubin¹⁸ , Molly R. Kosiarek^{23,51} , Michael B. Lund⁵ , Jessie L. Christiansen⁵ , Rachel A. Matson²⁵ , Charles A. Beichman⁵ , Joshua E. Schlieder²⁶ , Erica J. Gonzales^{27,53} , César Briceño²⁸ , Nicholas Law²⁹ , Andrew W. Mann²⁹ , Kevin I. Collins³⁰ , Phil Evans³¹ , Akihiko Fukui^{32,33} , Eric L. N. Jensen³⁴ , Felipe Murgas^{35,36} , Norio Narita^{35,37,38,39} , Enric Pallé^{35,36} , Hannu Parviainen^{35,36} , Richard P. Schwarz⁴⁰ , Thiam-Guan Tan⁴¹ , Jack S. Acton⁴² , Edward M. Bryant⁴³ , Alexander Chaushev⁴⁴ , Sam Gill⁴³ , Philipp Eigmüller⁴⁵ , Jon Jenkins⁸ , George Ricker⁴⁶ , Sara Seager^{47,48,49} , and Joshua N. Winn⁵⁰

¹Institute for Astronomy, University of Hawai'i, 2680 Woodlawn Drive, Honolulu, HI 96822, USA

²Division of Geological and Planetary Sciences, 1200 E. California Boulevard, Pasadena, CA, 91125, USA

³Department of Physics and Astronomy, San Francisco State University, 1600 Holloway Avenue, San Francisco, CA 94132, USA

⁴Center for Astrophysics | Harvard & Smithsonian, 60 Garden Street, Cambridge, MA 02138, USA

⁵NASA Exoplanet Science Institute, Caltech/IPAC, Pasadena, CA 91125, USA

⁶Observatoire de l'Université de Genève, 51 Chemin des Maillettes, 1290 Versoix, Switzerland

⁷Dunlap Institute for Astronomy and Astrophysics, University of Toronto, 50 St. George Street, Toronto, Ontario M5S 3H4, Canada

⁸NASA Ames Research Center, Moffett Field, CA 94035, USA

⁹Department of Astronomy and Astrophysics, University of California, Santa Cruz, CA 95060, USA

¹⁰Department of Physics & Astronomy, University of Kansas, 1082 Malott, 1251 Wescoe Hall Drive, Lawrence, KS 66045, USA

¹¹501 Campbell Hall, University of California at Berkeley, Berkeley, CA 94720, USA

¹²NASA Exoplanet Science Institute/Caltech-IPAC, MC 314-6, 1200 E. California Boulevard, Pasadena, CA 91125, USA

¹³Department of Astronomy, California Institute of Technology, Pasadena, CA 91125, USA

¹⁴Department of Astronomy, University of California Berkeley, Berkeley CA 94720, USA

¹⁵Centre for Astrophysics, University of Southern Queensland, Toowoomba, QLD, Australia

¹⁶Department of Earth and Planetary Sciences, University of California, Riverside, CA 92521, USA

¹⁷Department of Physics & Astronomy, University of California Los Angeles, Los Angeles, CA 90095, USA

¹⁸Department of Physics & Astronomy, University of California Irvine, Irvine, CA 92697, USA

¹⁹SETI Institute, Mountain View, CA 94043, USA

²⁰Vanderbilt University, Department of Physics & Astronomy, 6301 Stevenson Center Lane, Nashville, TN 37235, USA

²¹Department of Astronomy, University of California Berkeley, Berkeley, CA 94720, USA

²²Gemini Observatory, Northern Operations Center, 670 N. A'ohoku Place, Hilo, HI 96720, USA

²³Department of Astronomy and Astrophysics, University of California, Santa Cruz, CA 95064, USA

²⁴Division of Geological and Planetary Science, California Institute of Technology, Pasadena, CA 91125, USA

²⁵US Naval Observatory, 3450 Massachusetts Avenue NW, Washington, DC 20392, USA

²⁶Exoplanets and Stellar Astrophysics Laboratory, Mail Code 667, NASA Goddard Space Flight Center, Greenbelt, MD 20771, USA

²⁷University of California, Santa Cruz, 1156 High Street, Santa Cruz, CA 95064, USA

²⁸Cerro Tololo Inter-American Observatory, Casilla 603, La Serena 1700000, Chile

²⁹Department of Physics and Astronomy, The University of North Carolina at Chapel Hill, Chapel Hill, NC 27599-3255, USA

³⁰George Mason University, 4400 University Drive, Fairfax, VA 22030, USA

³¹El Sauce Observatory, Coquimbo Province, Chile

³²Department of Earth and Planetary Science, Graduate School of Science, The University of Tokyo, 7-3-1 Hongo, Bunkyo-ku, Tokyo 113-0033, Japan

³³Instituto de Astrofísica de Canarias, Vía Láctea s/n, E-38205 La Laguna, Tenerife, Spain

³⁴Dept. of Physics & Astronomy, Swarthmore College, Swarthmore PA 19081, USA

³⁵Instituto de Astrofísica de Canarias (IAC), 38205 La Laguna, Tenerife, Spain

³⁶Departamento de Astrofísica, Universidad de La Laguna (ULL), 38206, La Laguna, Tenerife, Spain

³⁷Komaba Institute for Science, The University of Tokyo, 3-8-1 Komaba, Meguro, Tokyo 153-8902, Japan

³⁸JST, PRESTO, 3-8-1 Komaba, Meguro, Tokyo 153-8902, Japan

³⁹Astrobiology Center, 2-21-1 Osawa, Mitaka, Tokyo 181-8588, Japan

⁴⁰Patashnick Voorheesville Observatory, Voorheesville, NY 12186, USA

⁴¹Perth Exoplanet Survey Telescope, Perth, Western Australia, Australia

⁴²School of Physics and Astronomy, University of Leicester, University Road, Leicester, LE1 7RH, UK

⁴³Department of Physics, University of Warwick, Gibbet Hill Road, Coventry CV4 7AL, UK

⁴⁴Center for Astronomy and Astrophysics, TU Berlin, Hardenbergstr. 36, D-10623 Berlin, Germany

⁴⁵Institute of Planetary Research, German Aerospace Center, Rutherfordstrasse 2, D-12489 Berlin, Germany

⁴⁶Kavli Institute for Astrophysics and Space Research, Massachusetts Institute of Technology, Cambridge, MA 02139, USA

⁴⁷Department of Physics and Kavli Institute for Astrophysics and Space Research, Massachusetts Institute of Technology, Cambridge, MA 02139, USA

⁴⁸Department of Earth, Atmospheric and Planetary Sciences, Massachusetts Institute of Technology, Cambridge, MA 02139, USA

⁴⁹ Department of Aeronautics and Astronautics, Massachusetts Institute of Technology, 77 Massachusetts Avenue, Cambridge, MA 02139, USA⁵⁰ Department of Astrophysical Sciences, Princeton University, 4 Ivy Lane, Princeton, NJ 08544, USA

Received 2020 September 4; revised 2020 December 7; accepted 2020 December 14; published 2021 January 11

Abstract

We report the discovery of TOI-561, a multiplanet system in the galactic thick disk that contains a rocky, ultra-short-period planet. This bright ($V = 10.2$) star hosts three small transiting planets identified in photometry from the NASA TESS mission: TOI-561 b (TOI-561.02, $P = 0.44$ days, $R_p = 1.45 \pm 0.11 R_\oplus$), c (TOI-561.01, $P = 10.8$ days, $R_p = 2.90 \pm 0.13 R_\oplus$), and d (TOI-561.03, $P = 16.3$ days, $R_p = 2.32 \pm 0.16 R_\oplus$). The star is chemically ($[\text{Fe}/\text{H}] = -0.41 \pm 0.05$, $[\alpha/\text{Fe}] = +0.23 \pm 0.05$) and kinematically consistent with the galactic thick-disk population, making TOI-561 one of the oldest (10 ± 3 Gyr) and most metal-poor planetary systems discovered yet. We dynamically confirm planets b and c with radial velocities from the W. M. Keck Observatory High Resolution Echelle Spectrometer. Planet b has a mass and density of $3.2 \pm 0.8 M_\oplus$ and $5.5^{+2.0}_{-1.6} \text{ g cm}^{-3}$, consistent with a rocky composition. Its lower-than-average density is consistent with an iron-poor composition, although an Earth-like iron-to-silicates ratio is not ruled out. Planet c is $7.0 \pm 2.3 M_\oplus$ and $1.6 \pm 0.6 \text{ g cm}^{-3}$, consistent with an interior rocky core overlaid with a low-mass volatile envelope. Several attributes of the photometry for planet d (which we did not detect dynamically) complicate the analysis, but we vet the planet with high-contrast imaging, ground-based photometric follow-up, and radial velocities. TOI-561 b is the first rocky world around a galactic thick-disk star confirmed with radial velocities and one of the best rocky planets for thermal emission studies.

Unified Astronomy Thesaurus concepts: Exoplanets (498); Exoplanet astronomy (486); Exoplanet systems (484); Exoplanet detection methods (489); Exoplanet structure (495); Exoplanet formation (492); Exoplanet evolution (491)

Supporting material: machine-readable table

1. Introduction

The NASA Kepler mission demonstrated that small planets are abundant in the Milky Way (Borucki et al. 2010; Howard et al. 2012; Fressin et al. 2013; Petigura et al. 2013). What are the properties of small planets around nearby, bright stars, including their bulk and atmospheric compositions? How do planet properties vary with stellar type and age? The NASA TESS mission is a two-year, all-sky survey that is finding small, transiting planets around nearby F-, G-, K-, and M-type stars (Ricker et al. 2015). The all-sky strategy enables TESS to sample the transiting planets around brighter stars spanning a wider range of properties than were represented in the pencil-beam Kepler survey.

A TESS mission level-one science goal is to measure the masses of 50 sub-Neptune-size transiting planets.⁵⁴ The TESS-Keck Survey (TKS) is a multi-institutional collaboration of Keck-HIRES users who are pooling Keck-HIRES time to meet this science goal and others (see TKS-I, Dalba et al. 2020; and also TKS-0, A. Chontos et al. 2021, in preparation). The TKS science goals include determining the masses, bulk densities, orbits, and host-star properties of planets in our survey. Our survey targets were selected to answer broad questions about planet properties, formation, and evolution.

TESS Object of Interest (TOI) 561 is a $V = 10.2$ star that advances three of the TKS science goals: (1) to compare planetary siblings in systems with multiple transiting planets, (2) to characterize ultra-short-period planets (USPs), and (3) to study planetary systems across a variety of stellar types. Systems with multiple transiting planets provide excellent natural laboratories for testing the physics of planet formation because the planets all formed around the same star and from

the same protoplanetary disk. TOI-561 is a bright star for which planet masses, interior compositions, and eventually atmospheric compositions can be determined through follow-up efforts. Our investigation of TOI-561 advances our goal to compare the fundamental physical properties of small-planet siblings in extrasolar systems.

TOI-561 also hosts a USP that has an orbital period of < 1 day and a radius consistent with a rocky composition (e.g., Weiss & Marcy 2014; Rogers 2015).⁵⁵ The present-day location of USPs corresponds to the former evacuated region of the protoplanetary disk. Because the protoplanetary disk cavity forms during the first few million years of the star's existence, this inner region should have been depleted of the building blocks necessary to assemble planets. Thus, the formation of USPs is poorly understood but likely involves migration to overcome the low local density of solids. Characterizing the mass and bulk density of TOI-561 b clarifies how it and other USPs formed.

We did not initially select TOI-561 for its host-star properties, but we discovered during our investigation that TOI-561 is a member of the galactic thick disk. Its low metallicity, high alpha abundance, and old age make it a special case that may advance our understanding of both multiplanet systems and the formation of USPs. Its unusual chemistry, kinematics, and age also address a third goal of TKS, which is to study planetary systems across a variety of stellar types.

In Section 2, we describe the TESS photometry, including the signals of the three transiting planet candidates. In Section 3, we characterize the host star. We describe our methods of planet candidate validation with ground-based photometry (Section 4) and high-resolution imaging (Section 5), and confirmation with radial velocities (RVs; Section 6). We describe the planet masses and densities in Section 7. We discuss the planetary system orbital

⁵¹ NSF Graduate Research Fellow.⁵² NSF Astronomy and Astrophysics Postdoctoral Fellow.⁵³ National Science Foundation Graduate Research Fellow.⁵⁴ NASA TESS mission, accessed 2020 August 23: <https://heasarc.gsfc.nasa.gov/docs/teess/primary-science.html>.⁵⁵ The definition of USPs as having $P < 1$ day is somewhat arbitrary; see Sanchis-Ojeda et al. (2014) versus Dai et al. (2018).

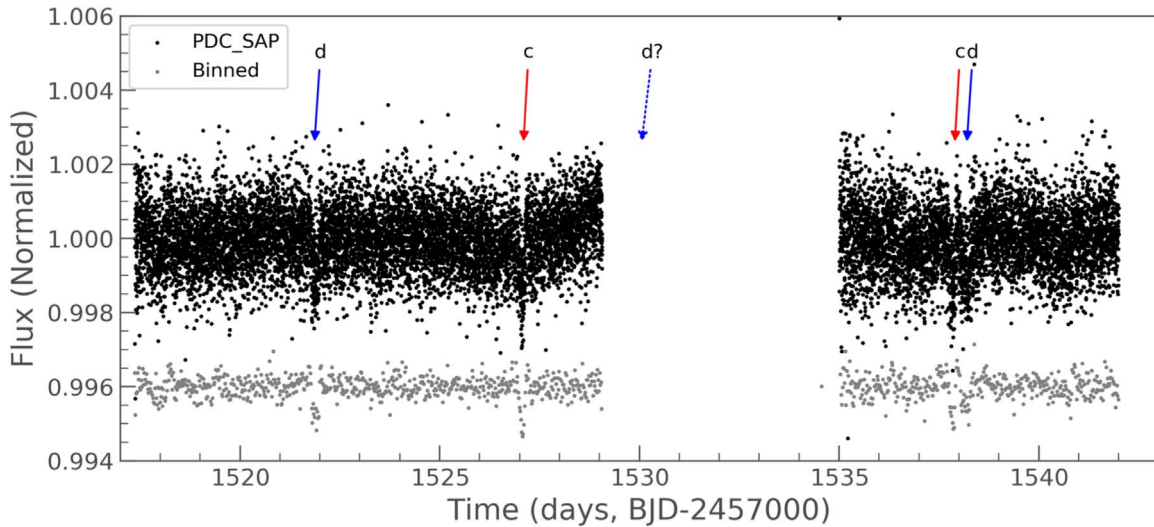


Figure 1. The presearch data conditioning SAP TESS photometry of TOI-561 (black points) and the same photometry but binned every 13 data points and flattened with a Savitzky–Golay filter (Savitzky & Golay 1964, gray points, with flux offset). Individual transits of planets c (red arrows) and d (blue arrows) are marked. A third transit of planet d could have occurred in the time-series gap (blue dotted arrow). A planet at $P = 0.44$ days (planet b) is also present, but the transits are too shallow to see in these data (see Figures 6 and 8).

dynamics and prospects for future atmospheric characterization in Section 8. We conclude in Section 9.

2. TESS Photometry

The vetting team of the TESS Science Processing Operations Center (SPOC) identified three transiting planets in their analysis of the photometry for TESS Input Catalog (TIC) ID 377064495 (Jenkins et al. 2016; Twicken et al. 2018; Li et al. 2019). The presearch data conditioning simple aperture photometry (PDCSAP) is shown in Figure 1 (Smith et al. 2012; Stumpe et al. 2012, 2014). The star was observed in Sector 8 at a 2 minute cadence. The SPOC-defined aperture is overlaid on the target in a Full-Frame Image (FFI) in Figure 2. The first planet candidate the SPOC pipeline detected is at $P = 10.78$ days (TOI-561.01, planet c) based on two transits, with signal-to-noise ratio (S/N) 9.8. After masking the flux near the transits of planet c, the SPOC pipeline detected a planet candidate at $P = 0.45$ days (TOI-561.02, planet b) based on 55 transits, with S/N 10.0. After masking the flux near transits of both planets c and b, the SPOC pipeline detected a planet candidate at $P = 16.4$ days (TOI-561.03, planet d⁵⁶), which transits twice, with S/N 9.2.

Several attributes of the TESS photometry complicate our analysis, particularly for planet d. There is a gap partway through the time series that creates an alias in our interpretation of the transit signals. The timing of the gap corresponds to a data download and also an unplanned interruption in communication between the instrument and spacecraft.⁵⁷ The USP transited 55 times during the TESS observations, leading to a robust ephemeris determination (although individual transits are too shallow to identify by eye in the photometry; see Section 4 for the phase-folded photometry and Section 6 for the RV planet confirmation). However, only two transits of planet c and two transits of planet d were detected. The transits of c

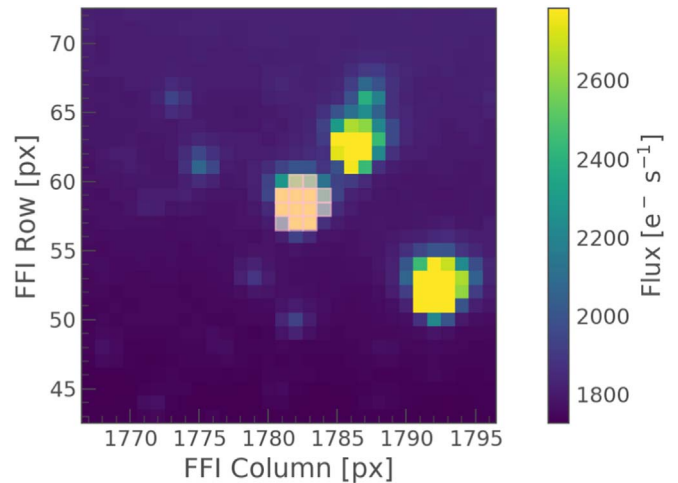


Figure 2. The TESS Full-Frame Image centered on TOI-561. The SPOC-defined aperture is a pale pink overlay on the central star. The TESS plate scale is $21''$ per pixel. The target star has TESS magnitude 9.49. False-positive scenarios in which the bright nearby stars are eclipsing binaries, with some flux contaminating the target pixels, are ruled out with the data validation centroid test (planet d) and/or follow-up ground-based photometry (Section 4, planets b and c).

and d occurred on different sides of the data gap. For planet c, the nondetection of additional transits in the TESS photometry leads to a robust determination of the orbital period at 10.78 days, but, for planet d, periods of 16 days (there is no transit during the gap) or 8 days (there is a transit in the gap; see the dotted blue arrow in Figure 1).

Another challenge is that the second transit of planet d overlaps with a transit of planet b and is near a transit of planet c, and so much of the photometry during and near the second transit of d was masked in the original pipeline. The lack of a photometric continuum around the transit makes it difficult to isolate it and determine an accurate midtime, depth, and duration.

To mitigate the frequent gaps from masking planets b and c, we ran a custom iteration of the SPOC data validation (DV)

⁵⁶ This planet is labeled planet f in the NASA Exoplanet Archive to distinguish it from the planets d and e reported by Lacedelli et al. (2020).

⁵⁷ TESS Data Release Notes: Sector 8, DR10, https://archive.stsci.edu/missions/teess/doc/teess_dr10/teess_sector_08_dr10_v02.pdf.

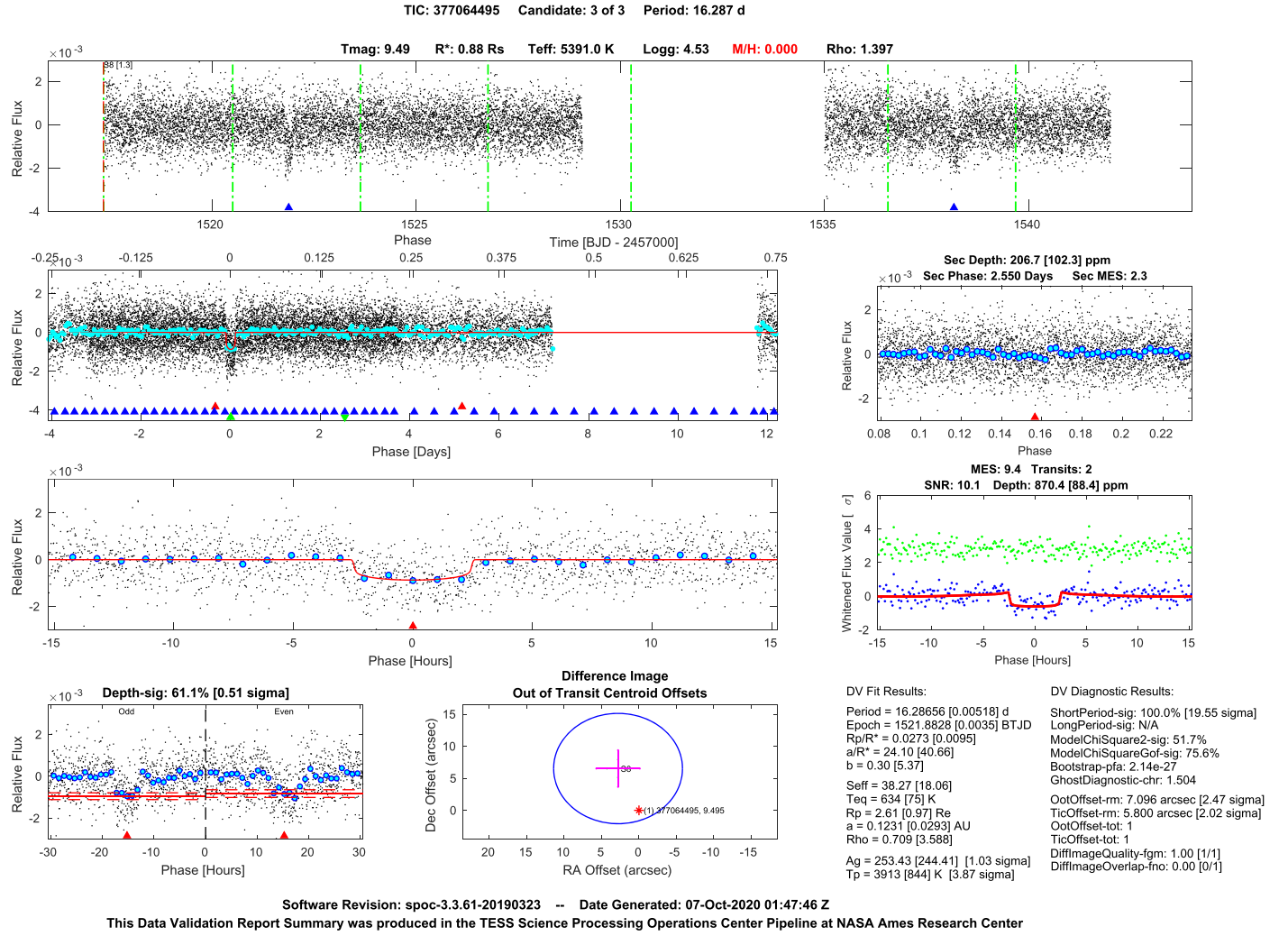


Figure 3. A custom run of the SPOC pipeline and DV analysis for TOI-561 provided more robust parameters than the default SPOC analysis. In the default analysis, the transits of planet d were affected by many short data gaps that resulted from masking the transits of b and c. In our custom analysis, we subtracted (instead of masking) the transits of planets b and c, finding $P_d = 16.29$ days (instead of 16.37 days). The depths and durations of the two transits of planet d (bottom-left panel) are consistent to $< 1\sigma$.

pipeline (Figure 3). We first identified planets c and b but subtracted the best-fit models rather than masking the transits entirely so that we did not remove valuable continuum or in-transit data from the region with overlapping transits. We then identified and fit planet d. In our custom DV analysis, the depth for the odd transit of planet d is 947 ± 126 ppm and the depth for the even transit is 856 ± 124 ppm. The duration for the odd transit is 5.06 ± 0.57 hours, and the duration for the even transit is 5.62 ± 0.62 hours. The difference in the odd versus even transit depths is 0.51σ , and the difference in the odd versus even transit durations is 0.66σ . The transit depths from our custom DV analysis are consistent with the values from the original report.

A key difference between the original pipeline and our custom analysis is that the original SPOC pipeline identified the time between the two transits of planet d as 16.37 days, whereas in our custom analysis, that interval is 16.29 days. The partial masking of planet d’s transit in the original pipeline likely caused an inaccurate transit midpoint determination for the second transit, producing the inaccurate orbital period. Our revised orbital period of 16.29 days implies that several

follow-up photometric efforts for planet d were off by > 1 day (Section 4).

Despite the challenges related to planet d, the three planet candidates performed well in the DV diagnostic tests. The candidates passed all of the tests except for the difference image centroiding test, which placed the source for 561 b within $11''$, 561 c within $23''$, and 561 d within $7''$ (and a passing score for this test). They all passed the ghost diagnostic test as well, indicating that if they were due to background eclipsing binaries, the offending star would have to be within a pixel of the location of the target star. All three planet candidates pass the SPOC pipeline odd–even test, with insignificant differences between the depths of odd-numbered versus even-numbered transits.⁵⁸

The combination of DV and ground-based follow-up is sufficient to rule out a broad variety of astrophysical false-positive scenarios for the planets. Planet d passes the centroiding test in the DV report, ruling out a nearby eclipsing

⁵⁸ In the scenario of an 8 day period for planet d, the odd–even test is not meaningful, as the two transit-like events would correspond to two odd-numbered events.

binary (NEB) as the source of the transits. Through ground-based photometry, we recovered additional on-target transits of planet c, and also ruled out an NEB as the source of the transits for planet b (Section 4). Ground-based high-resolution imaging (Section 5) rules out background eclipsing binary false positives for all three planets. RVs (Section 6) rule out that the target star itself is a spectroscopic eclipsing binary, and we detect planetary-mass RV signals at the ephemerides of planets b and c.

3. Stellar Properties

3.1. High-resolution Spectroscopy

We obtained a high signal-to-noise spectrum at $R = 60,000$ (Section 6) of TOI-561 to determine atmospheric parameters and detailed chemical abundances using the line list and forward modeling procedure of Brewer et al. (2016). The modeling uses Spectroscopy Made Easy (SME; Valenti & Piskunov 1996; Piskunov & Valenti 2017) in an iterative scheme that alternates between solving for global stellar properties and a detailed abundance pattern. We begin by estimating T_{eff} from $B-V$ colors then fitting for T_{eff} , $\log g$, $[M/H]$, Doppler line broadening, and the abundances of the α elements calcium, silicon, and titanium. All other elements are scaled solar values based on the overall metallicity given by $[M/H]$ and the initial abundances are set to solar. The temperature of the resulting model is perturbed by ± 100 K and used as input to refit the spectrum. The χ^2 weighted average of the global stellar parameters is then fixed and used as the input for the next step of simultaneously fitting for the abundances of 15 elements.

Simultaneous fitting of the elements is critical in obtaining precise abundances due to chemical processes in the stellar photosphere (e.g., Ting et al. 2018). The formation of molecules in cooler stars, even in very low numbers, can alter the atomic number densities and hence measured abundances using only isolated atomic lines.

The global parameters and abundance pattern obtained in the first iteration are then used as an initial guess for a second fitting following the same steps. Finally, the macroturbulence is set using a T_{eff} relation from Brewer et al. (2016), and we solve for the projected rotational velocity, $v \sin i$, with all other parameters fixed. The resulting gravities have been shown to be consistent with those from asteroseismology to within 0.05 dex and the abundance uncertainties are between 0.01 and 0.04 dex (Brewer et al. 2015). An empirical correction is applied to the abundances as a function of temperature (Brewer et al. 2016), which adds additional uncertainty to the absolute abundance, especially at temperatures between 5000 and 5500 K, and we adopt 0.05 dex uncertainty for most elements. Our analysis yielded a low stellar metallicity and high α abundance ($[Fe/H] = -0.41 \pm 0.05$, $[\alpha/Fe] = +0.23 \pm 0.05$, see Table 1).

The effective temperature derived from the SME analysis (5326 ± 25 K)⁵⁹ is in good agreement with alternative estimates using SpecMatch Synth (5249 ± 110 K; Petigura 2015), SpecMatch-Emp (5302 ± 110 K; Yee et al. 2017), and color- T_{eff} relations applied in the TESS Input Catalog (5440 ± 110 K; Stassun et al. 2018), and applying a $J-K$ color- T_{eff} relation (5300 ± 110 K, Casagrande et al. 2010). We adopted the SME-derived solution, with an error bar calculated from the

Table 1
Host-star Characteristics

Basic Properties	
Tycho ID	243-1528-1
TIC ID	377064495
Gaia DR2 ID	3850421005290172416
R.A.	09:52:44.44
Decl.	+06:12:57.00
Tycho V_T Magnitude	10.25
TESS Magnitude	9.49
2MASS K Magnitude	8.39
Gaia DR2 Astrometry	
Parallax, π (mas)	11.627 ± 0.067
Radial Velocity (km s ⁻¹)	79.54 ± 0.56
Proper Motion in RA (mas yr ⁻¹)	-108.432 ± 0.088
Proper Motion in DEC (mas yr ⁻¹)	-61.511 ± 0.094
High-resolution Spectroscopy	
Effective Temperature, T_{eff} (K)	5326 ± 64
Surface Gravity, $\log g$ (cm s ⁻²)	4.52 ± 0.05
Projected rotation speed, $v \sin i$ (km s ⁻¹)	< 2.0
$\log R'_{\text{HK}}$ (dex)	-5.1
Iron Abundance, $[Fe/H]$ (dex)	-0.41 ± 0.05
Carbon Abundance, $[C/H]$ (dex)	-0.19 ± 0.05
Nitrogen Abundance, $[N/H]$ (dex)	-0.51 ± 0.05
Oxygen Abundance, $[O/H]$ (dex)	$+0.09 \pm 0.05$
Sodium Abundance, $[Na/H]$ (dex)	-0.39 ± 0.05
Magnesium Abundance, $[Mg/H]$ (dex)	-0.20 ± 0.05
Aluminum Abundance, $[Al/H]$ (dex)	-0.19 ± 0.05
Silicon Abundance, $[Si/H]$ (dex)	-0.24 ± 0.05
Calcium Abundance, $[Ca/H]$ (dex)	-0.27 ± 0.05
Titanium Abundance, $[Ti/H]$ (dex)	-0.20 ± 0.05
Vanadium Abundance, $[V/H]$ (dex)	-0.27 ± 0.05
Chromium Abundance, $[Cr/H]$ (dex)	-0.43 ± 0.05
Manganese Abundance, $[Mn/H]$ (dex)	-0.60 ± 0.05
Nickel Abundance, $[Ni/H]$ (dex)	-0.37 ± 0.05
Yttrium Abundance, $[Y/H]$ (dex)	-0.42 ± 0.05
Alpha Abundance, $[\alpha/Fe]$ (dex)	$+0.23 \pm 0.05$
Distance Modulus and Isochrone Modeling	
Stellar Luminosity, L_* (L_{\odot})	0.522 ± 0.017
Stellar Mass, M_* (M_{\odot})	0.805 ± 0.030
Stellar Radius, R_* (R_{\odot})	0.832 ± 0.019
Stellar Density, ρ_* (ρ_{\odot})	1.38 ± 0.11
Surface Gravity, $\log g$ (cgs)	4.500 ± 0.030
Age (Gyr)	10 ± 3
Transit Modeling	
Limb Darkening (TESS band), q_1	$0.2^{+0.2}_{-0.2}$
Limb Darkening (TESS band), q_2	$0.4^{+0.3}_{-0.2}$

Note. The TESS magnitude is adopted from the TESS Input Catalog (Stassun et al. 2018), and the kinematics are taken from Gaia DR2 (Lindegren et al. 2018). Stellar parameters from isochrone modeling are formal uncertainties only and do not incorporate systematic errors from different model grids. The transit modeling is described in Section 4.

standard deviation of T_{eff} estimates from different methods: 5326 ± 64 K.

For each spectrum, we measure the Mt. Wilson S value, an indicator of the chromospheric magnetic activity. The Mt. Wilson S value is a measure of the strength of the emission cores in the Ca II H and K lines relative to the nearby

⁵⁹ This error is the formal uncertainty, not the adopted error.

Table 2
Radial Velocities

Time (BJD)	RV (m s ⁻¹)	RV unc. (m s ⁻¹)	S val
2458599.74193	3.9	1.3	0.148
2458610.76476	1.3	1.4	0.147
2458617.75866	-1.9	1.4	0.142
2458622.74736	2.3	1.2	0.146
2458623.75550	2.9	1.4	0.146
2458627.75794	-6.5	1.6	0.151

Note. The first few lines are shown for form and content. The full machine-readable table is available.

(This table is available in its entirety in machine-readable form.)

continuum flux. Our procedure for determining the S values is described in Isaacson & Fischer (2010). See Section 6, Table 2, for the full S -value time series. A Lomb-Scargle periodogram of the S values results in peaks near 100 days and 230 days, neither of which is near the expected rotation period or magnetic activity cycle of this old K dwarf (Section 6).

3.2. Distance Modulus and Isochrone Modeling

The stellar atmosphere and interior models are typically calculated using a solar-scaled α -element abundance mixture and thus assume $[\text{Fe}/\text{H}] = [\text{M}/\text{H}]$. To account for the nonsolar α abundances of TOI-561, we averaged the individual abundance measurements for $[\text{Mg}/\text{H}]$, $[\text{Si}/\text{H}]$, $[\text{Ca}/\text{H}]$, and $[\text{Ti}/\text{H}]$ to derive $[\alpha/\text{Fe}] = +0.23 \pm 0.05$, and then applied the calibration by Salaris et al. (1993) to convert the measured $[\text{Fe}/\text{H}]$ value into an overall metal abundance, yielding $[\text{M}/\text{H}] = -0.24 \pm 0.10$:

$$[\text{M}/\text{H}] = [\text{Fe}/\text{H}] + \log_{10}(0.694 \times 10^{[\alpha/\text{Fe}]} + 0.306). \quad (1)$$

We adopted a conservative uncertainty of 0.1 dex for $[\text{M}/\text{H}]$ to account for potential systematics in the Salaris et al. (1993) calibration.

Next, we used T_{eff} , $[\text{M}/\text{H}]$, $\log g$, Gaia DR2 parallax (adjusted for the 0.082 ± 0.033 mas zero-point offset for nearby stars reported by Stassun & Torres 2018), 2MASS K -band magnitude, a 3D dust map, and bolometric corrections to calculate a luminosity by solving the standard distance modulus, as implemented in the “direct mode” of *isoclassify* (Huber et al. 2017). We then combined the derived luminosity with T_{eff} and $[\text{M}/\text{H}]$ to infer additional stellar parameters (mass, radius, density) using the “grid mode” of *isoclassify*, which performs a probabilistic inference of stellar parameters using a grid of MIST isochrones (Choi et al. 2016). The isochrone-derived $\log g$ (4.50 ± 0.03 dex) is in excellent agreement with spectroscopy (4.52 ± 0.05 dex), confirming that no additional iteration in the above steps is required for a self-consistent solution. The derived age of the isochrone fit is 10 ± 3 Gyr, consistent with the mean age of a galactic thick-disk star (see the following section).

The full set of stellar parameters is listed in Table 1. The results show that TOI-561 is an early-K dwarf with a radius of $R_{\star} = 0.832 \pm 0.019 R_{\odot}$ and mass $M_{\star} = 0.805 \pm 0.030 M_{\odot}$. We note that the quoted uncertainties are formal error bars and do not include potential systematic errors due to the use of different model grids (Tayar et al. 2021). For example, the stellar radius in Table 1 is 3% lower than predicted from an

application of the Stefan–Boltzmann law using either the “direct mode” of *isoclassify* or SED fitting (Stassun et al. 2017), both of which yield $0.86 \pm 0.02 R_{\odot}$. However, this 3% ($\approx 1 \sigma$) difference does not significantly affect our main conclusions on the properties of the planets in the TOI-561 system, because the planet density errors are dominated by uncertainties in the planet masses (see Section 7).

We used the stellar evolution model fitting tool *kiauhoku* (Clayton et al. 2020) to estimate the rotation period of TOI-561. Using the stellar T_{eff} , $[\text{Fe}/\text{H}]$, and $[\alpha/\text{Fe}]$ from Table 1 as inputs and assuming an age of 10 ± 3 Gyr, we found two different model-dependent estimates of the rotation period. Assuming the magnetic braking law described in van Saders & Pinsonneault (2013), we found $P_{\text{rot}} = 38.5 \pm 7.3$ days, but assuming the stalled-braking law of van Saders et al. (2016), we found $P_{\text{rot}} = 35.7 \pm 3.4$ days. These rotation periods are consistent with the upper limit of $v \sin i$ we determined spectroscopically. However, the estimated rotation periods differ significantly from the periodicity identified in the Mt. Wilson S -value activity indices (see Table 2), suggesting that the rotation period is not detected in the S -value time series. A rotation period of >30 days is likely too long to identify in the single sector of TESS photometry. We checked the archives of several ground-based photometric surveys, but TOI-561 saturates in ASAS-SN and Pan-STARRS, and it is too close to the equator to be included in WASP.

3.3. Galactic Evolution

Early studies of star counts in the Milky Way revealed two distinct populations in the galactic disk which dominate at different scale heights, commonly denoted the “thin” and “thick” disk population (Gilmore & Reid 1983). Spectroscopic and photometric surveys have shown that these populations can be approximately separated based on kinematics and chemical abundances, with thick-disk stars being kinematically hotter (e.g., Fuhrmann 1998), older (Bensby et al. 2005), more metal poor, and enriched in α -process elements (e.g., Fuhrmann 1998).

The formation of the thick disk is still debated, with scenarios including external processes such as the accretion of stars from the disruption of a satellite galaxy (e.g., Abadi et al. 2003) and induced star formation from mergers with other galaxies (e.g., Brook et al. 2004), or a natural dynamical evolution of our galaxy including radial migration (Schönrich & Binney 2009a, 2009b). While the mere existence of a distinct thick disk is still in question (Bovy et al. 2012), spectroscopic and asteroseismic surveys have confirmed that chemically identified “thick-disk” stars belong to the old population of our galaxy, with typical ages of ~ 11 Gyr (Silva Aguirre et al. 2018).

The detection of exoplanets around different galactic stellar populations can provide powerful insights into their formation and evolution (Adibekyan et al. 2012). For example, the discovery of five sub-Earth-size planets orbiting the thick-disk star Kepler-444 (Campante et al. 2015) demonstrated for the first time that terrestrial planet formation has occurred for at least ~ 11 Gyr, and the discovery of a close M-dwarf binary companion demonstrated that this process can even proceed in a truncated protoplanetary disk (Dupuy et al. 2016). While TESS probes nearby stellar populations, it has significant potential to expand this sample. Indeed, Gan et al. (2020) recently presented the first TESS exoplanet orbiting a thick-disk star identified based on kinematics.

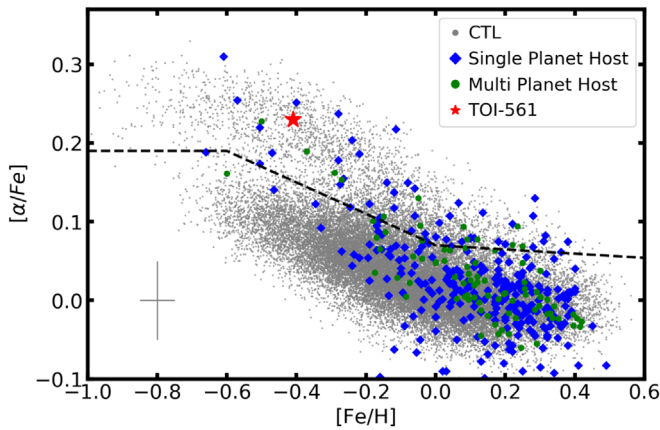


Figure 4. Iron abundance vs. $[\alpha/\text{Fe}]$ for stars in the TESS candidate target list (CTL) observed by the GALAH survey (De Silva et al. 2015; Sharma et al. 2018) and a sample of exoplanet host stars taken from Hypatia catalog (Hinkel et al. 2014). Known exoplanet hosts are separated into those with a single known planet (blue diamonds) and multiple known planets (green circles). The position of TOI-561 is marked by a red star. The black dashed line approximately separates the galactic thin-disk and thick-disk populations.

Figure 4 compares the chemical properties of TOI-561 with a sample of field stars in the TESS candidate target list (CTL) observed by the GALAH survey (De Silva et al. 2015; Sharma et al. 2018) and a sample of known exoplanet hosts from the Hypatia catalog (Hinkel et al. 2014). We calculated $[\alpha/\text{Fe}]$ for stars in the Hypatia catalog in the same manner as for TOI-561 and discarded stars with abundance uncertainties > 0.2 dex (calculated from the scatter between different methods). TOI-561 is consistent with the thick disk in terms of its chemical abundances, in agreement with the high proper motions measured by Gaia (Table 1) and the kinematic classification of TOI-561 by Carrillo et al. (2020). To independently confirm the kinematic classification, we used the *UVW* velocity vector of TOI-561 via the online velocity calculator of Rodriguez (2016), finding $(U, V, W) = (-60.0, -70.9, +16.7) \text{ km s}^{-1}$. Using the probabilistic framework of Bensby et al. (2004) and Bensby et al. (2014), we find a thick-to-thin disk probability ratio of $TD/D = 19$, indicating strong evidence that this star is a member of the thick disk.

TOI-561 is the first chemically and kinematically confirmed thick-disk exoplanetary system discovered by TESS, the fifth known thick-disk star known to host multiple planets, and the first thick-disk star known to host an ultra-period short planet. This further demonstrates that (1) small, rocky planets can form in metal-poor environments (consistent with Buchhave et al. 2012), (2) USPs are not tidally destroyed around old stars (consistent with Hamer & Schlaufman 2020), and (3) rocky planets have been forming for nearly the age of the universe.

4. Time-series Photometric Follow-up and Analysis

We acquired ground-based time-series follow-up photometry of TOI-561 as part of the TESS Follow-up Observing Program (TFOP)⁶⁰ to attempt to (1) rule out NEBs as potential sources of the TESS detections and (2) detect the transits on target to refine the TESS ephemerides. We used the TESS Transit Finder, which is a customized version of the Tapir software package (Jensen 2013), to schedule our transit observations.

⁶⁰ TFOP website: <https://tess.mit.edu/followup>.

4.1. LCOGT

We observed TOI-561 using the Las Cumbres Observatory Global Telescope (LCOGT) 1 m networks (Brown et al. 2013) in the Pan-STARRS *z*-short (*zs*) band. The telescopes are equipped with 4096×4096 SINISTRO cameras having an image scale of $0''.389 \text{ pixel}^{-1}$ resulting in a $26' \times 26'$ field of view. The images were calibrated using the standard LCOGT BANZAI pipeline (McCully et al. 2018), and the photometric data were extracted using the AstroImageJ (AIJ) software package (Collins et al. 2017). A full transit window of TOI-561 b was observed continuously for 205 minutes on 2019 April 19 UT from the LCOGT Siding Spring Observatory (SSO) node. TOI-561 c was observed continuously for 381 minutes on 2020 February 3 UT from the LCOGT McDonald Observatory node and again on 2020 March 17 UT from the LCOGT Cerro Tololo Inter-American Observatory (CTIO) node for 230 minutes and then later on the same epoch from the LCOGT SSO node for 269 minutes. TOI-561 d was observed continuously for 300 minutes on 2020 April 24 UT from the LCOGT SSO node.

4.2. NGTS

The Next Generation Transit Survey (NGTS; Wheatley et al. 2018), located at ESO’s Paranal Observatory, is a photometric facility dedicated to hunting exoplanets. NGTS consists of 12 independently operated 20 cm diameter robotic telescopes, each with an 8 deg^2 field of view and a plate scale of $5'' \text{ pixel}^{-1}$. The NGTS telescopes also benefit from subpixel guiding afforded by the DONUTS autoguiding algorithm (McCormac et al. 2013). By using multiple NGTS telescopes to simultaneously observe the same star, NGTS can achieve ultra-high-precision light curves of exoplanet transits (Bryant et al. 2020; Smith et al. 2020).

TOI-561 was observed on two nights using NGTS multi-telescope observations. On UT 2020 February 2, a full transit of TOI-561 c was observed using three NGTS telescopes. A predicted transit ingress of TOI-561 d was observed on the night of UT 2020 March 5 using four NGTS telescopes. A total of 5179 images were obtained during the first observation and 7791 during the second. Both sets of observations were performed using an exposure time of 10 s and the custom NGTS filter (520–890 nm). The airmass of the target was kept below 2, and the sky conditions were good for all the observations.

We reduced the NGTS images using the custom aperture photometry pipeline detailed in Bryant et al. (2020). This pipeline performs source extraction and photometry using the SEP library (Bertin & Arnouts 1996; Barbary 2016). The pipeline also uses GAIA DR2 (Gaia Collaboration et al. 2016, 2018) to automatically identify a selection of comparison stars that are similar to TOI-561 in terms of brightness, color, and CCD position.

4.3. MuSCAT2

We observed full transit windows of TOI-561 b continuously for 120 minutes on 2019 April 23 UT and 2020 May 24 UT simultaneously in the *g*, *r*, *i*, and *z_s* bands with the MuSCAT2 multicolor imager (Narita et al. 2019) installed at the 1.52 m Telescopio Carlos Sanchez in the Teide Observatory, Spain. The photometry was carried out using standard aperture photometry calibration and reduction steps with a dedicated MuSCAT2 photometry pipeline, as described in Parviainen et al. (2020).

4.4. PEST

We observed a full transit window of TOI-561 b continuously for 205 minutes on 2019 April 22 UT in the R_c band from the Perth Exoplanet Survey Telescope (PEST) near Perth, Australia. The 0.3 m telescope is equipped with a 1530×1020 SBIG ST-8XME camera with an image scale of $1''.2 \text{ pixel}^{-1}$ resulting in a $31' \times 21'$ field of view. A custom pipeline based on C-Munipack⁶¹ was used to calibrate the images and extract the differential photometry.

4.5. El Sauce

We observed a full transit window of TOI-561 b continuously for 206 minutes on 2019 April 23 UT in the R_c band from El Sauce Observatory in Coquimbo Province, Chile. The 0.36 m Evans telescope is equipped with a 1536×1024 SBIG STT-1603-3 camera with an image scale of $1''.47 \text{ pixel}^{-1}$ resulting in an 18.8×12.5 field of view. The photometric data were extracted using AIJ.

4.6. TOI-561 b

The TOI-561 b SPOC pipeline transit depth is generally too shallow (290 ppm) for ground-based detection, so we checked all three stars within $2.5'$ that are bright enough to have caused the SPOC detection (i.e., TESS magnitude < 18.1) for a possible NEB that could be contaminating the SPOC photometric aperture. We estimate the expected NEB depth in each neighboring star by taking into account both the difference in magnitude relative to TOI-561 and the distance to TOI-561 (to estimate the fraction of the star's flux that would be contaminating the TESS aperture for TOI-561). If the rms of the 5 minute binned light curve of a neighboring star is more than a factor of 3 smaller than the expected NEB depth, we consider an NEB to be ruled out. We also visually inspect each star's light curve to ensure that there is no obvious eclipse-like signal, even though the rms to the estimated NEB depth threshold is met. Using a combination of the LCOGT, MuSCAT2, PEST, and El Sauce TOI-561 b follow-up observations, we rule out the possibility of a contaminating NEB at the SPOC pipeline ephemeris.

4.7. TOI-561 c

In the LCOGT observation of TOI-561 c on 2020 February 3 UT, we detected a 142 minute, early (0.3σ) ~ 1100 ppm egress, relative to the nominal SPOC ephemeris, in a $9''.7$ radius aperture around the target star, which is not contaminated by any known Gaia DR2 stars. NGTS observed and detected the same transit on time (Figure 5). As a result, we revised the follow-up orbital period to 10.778325 days for further scheduling. The 2020 March 17 UT LCOGT CTIO and SSO observations then detected an on-time ingress and egress, respectively, at the revised ephemeris.

4.8. TOI-561 d

The LCOGT observation of TOI-561 d on 2020 April 24 UT covered an egress ± 150 minutes relative to the nominal SPOC pipeline ephemeris and provides $\sim 1\sigma$ coverage of the original SPOC ephemeris uncertainty on the epoch of observation, but is 2 days away from the transit midpoint predicted by our

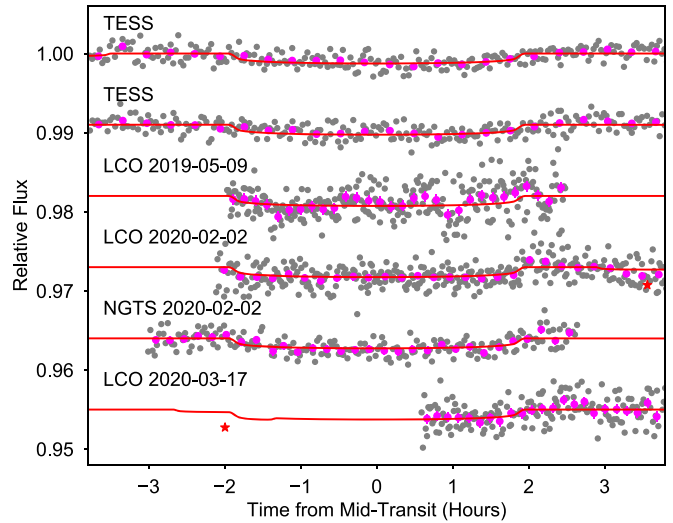


Figure 5. The individual transits of planet c from TESS and ground-based facilities. The magenta points are binned data. The red stars indicate the midtransits of planet b, which, due to the short orbital period, often overlap with the transits of planets c and d. The red solid line is the best-fit global model that includes both TESS and ground-based photometry and model transits of all three planets simultaneously. Note that the ground-based transits of planet d were acquired at times that are not consistent with our best-fit ephemeris, and they are not shown.

revised 16.29 day ephemeris. The LCOGT light curve does not show an obvious 923 ppm egress during the limited observation window. However, ingress- or egress-only coverage of transits with depths less than 1000 ppm from the LCOGT 1 m network can be difficult to interpret and reliably model due to potential trends in the data that may inject or mask a shallow ingress or egress. The NGTS observation on 2020 March 5 shows what might be the ingress of a transit of planet d. However, given the low S/N, this is not a high-confidence detection. Furthermore, if our revised 16.29 day ephemeris is correct, this observation was 2 days away from the transit midpoint.

4.9. Transit Modeling

Here we perform a joint analysis of TESS light curve and ground-based follow-up to refine the planetary parameters. We downloaded the TESS light curve from the Mikulski Archive for Space Telescopes (MAST; Figure 1). We isolated the transits of each planet with a window of three times the transit duration. We removed long-term stellar variability/instrumental effect by fitting a cubic spline with 1.5 day knot length to the light curve after removing the transits. We also downloaded the ground-based follow-up observations from the ExoFOP website⁶². We used the BATMAN (Kreidberg 2015) package for transit modeling, using the transit ephemerides reported by the TESS team as an initial guess for our model. Our model uses the mean stellar density ρ_* as a global parameter (with a Gaussian prior as derived in Section 3 and Table 1) on all three planets. For each planet, we allowed the radius ratio R_p/R_* , the impact parameter b , the orbital period P , and the midtransit time T_c to vary freely. We assumed circular orbits for all three planets. The mean stellar density ρ_* and the orbital period P together constrain the scaled semimajor axes a/R_* of each planet. We adopted a quadratic limb-darkening

⁶¹ <http://c-munipack.sourceforge.net>

⁶² <https://exofop.ipac.caltech.edu/teess/>

Table 3
Planet Parameters

Parameter	Median $\pm 1\sigma$
Planet b	
Orbital Period, P_b (days)	$0.446573^{+0.000032}_{-0.000021}$
Midtransit Time, T_c (BJD)	2458517.4973 ± 0.0018
Radius Ratio, R_p/R_*	0.016 ± 0.001
Impact Parameter, b	0.3 ± 0.2
Duration, T_{14} (hours)	1.42 ± 0.10
Orbital Eccentricity, e	0 (fixed)
RV Semiamplitude, K_b (m s^{-1})	3.1 ± 0.8
Semimajor axis, a_b (au)	0.01064 ± 0.00013
Radius, R_b (R_\oplus)	1.45 ± 0.11
Mass, M_b (M_\oplus)	3.2 ± 0.8
Density, ρ_b (g cm^{-3})	$5.5^{+2.0}_{-1.6}$
Equilibrium Temperature, $T_{\text{eq},b}$ (K)	2480 ± 200
Planet c	
Orbital Period, P_c (days)	10.77892 ± 0.00015
Midtransit Time, T_c (BJD)	$2458527.05825 \pm 0.00053$
Radius Ratio, R_p/R_*	0.032 ± 0.001
Impact Parameter, b	0.2 ± 0.2
Duration T_{14} (hours)	4.04 ± 0.26
Orbital Eccentricity, e	0 (fixed)
RV Semiamplitude, K_c (m s^{-1})	2.4 ± 0.8
Semimajor axis, a_c (au)	0.0888 ± 0.0011
Radius, R_c (R_\oplus)	2.90 ± 0.13
Mass, M_c (M_\oplus)	7.0 ± 2.3
Density, ρ_c (g cm^{-3})	1.6 ± 0.6
Equilibrium Temperature, $T_{\text{eq},c}$ (K)	860 ± 70
Planet d	
Orbital Period, P_d^a (days)	16.287 ± 0.005
Midtransit Time, T_c (BJD)	2458521.8828 ± 0.0035
Radius Ratio, R_p/R_*	0.0256 ± 0.0016
Impact Parameter, b	0.1 ± 0.1
Duration, T_{14} (hours)	4.45 ± 0.46
Orbital Eccentricity, e	0 (fixed)
RV Semiamplitude, K_d (m s^{-1})	0.9 ± 0.6
Semimajor axis, a_d^a (au)	0.1174 ± 0.0015
Radius, R_d (R_\oplus)	2.32 ± 0.16
Mass, M_d^a (M_\oplus)	$3.0^{+2.4}_{-1.9}$
Density, ρ_d^a (g cm^{-3})	$1.3^{+1.1}_{-0.8}$
Equilibrium Temperature, $T_{\text{eq},d}$ (K)	750 ± 60
Other	
RV Zero Point, γ (m s^{-1})	-0.8291
RV Jitter, σ_j (m s^{-1})	$4.09^{+0.49}_{-0.42}$

Note.

^a The orbital period of planet d was incorrectly identified as $P = 16.37$ days in the original SPOC pipeline because of a partially masked transit. An alias of the orbital period of planet d, $P_d = 8$ days, is also consistent with the data. Parameters marked with a dagger would be affected by an incorrect assumption of the orbital period of planet d. See Section 8 for assumptions regarding planet equilibrium temperatures.

law as parameterized by Kipping (2013). We allowed the coefficients q_1 and q_2 to vary in different photometric bands. We then performed a Monte Carlo Markov Chain analyses with the Python package emcee (Foreman-Mackey et al. 2013) to sample the posterior distribution of the various transit parameters. The results are summarized in Table 3, and Figure 6 shows the best-fit transit models.

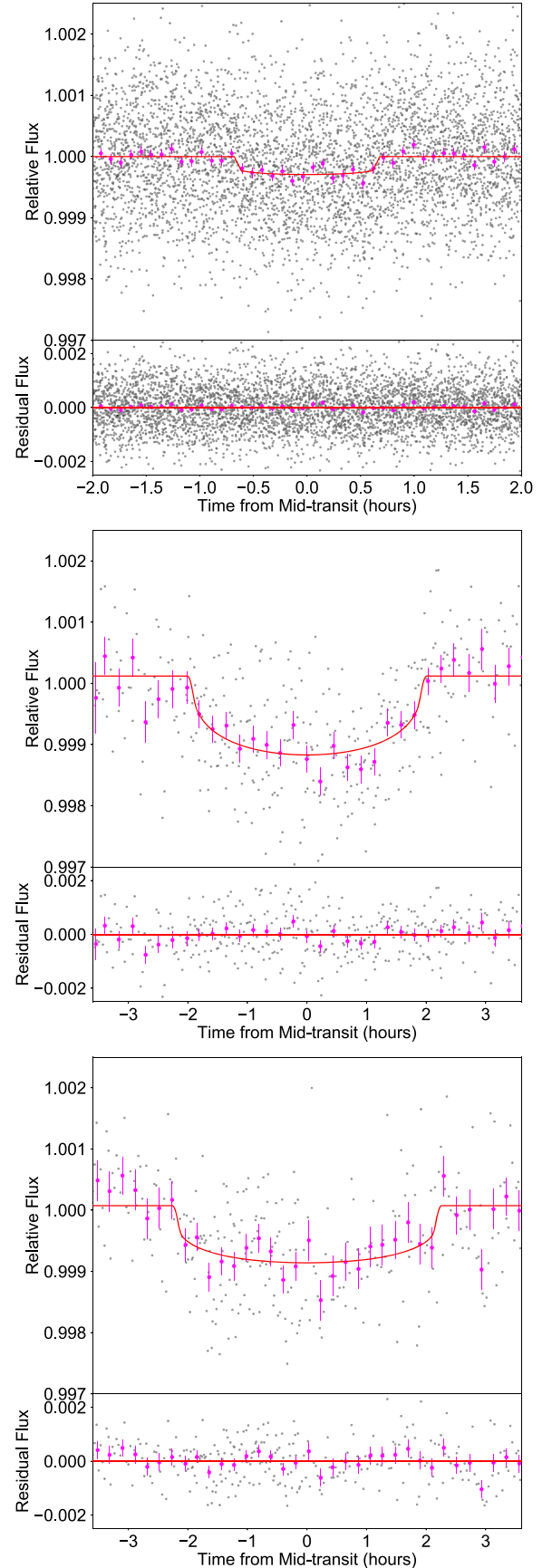


Figure 6. The phase-folded transits of TOI-561 planets b (top), c (middle), and d (bottom). We removed regions where two planets transit simultaneously before plotting. The magenta points show binned fluxes. The red solid line shows the best-fit transit models.

We found that the transit duration for d is long compared to what is expected for a planet in a circular, 16 day orbit, given the well-characterized stellar density.⁶³ The long transit duration can be resolved with a moderate eccentricity for planet d. We applied the photoeccentric method of Dawson et al. (2012) to estimate the eccentricity of planet d, finding $e_d = 0.24^{+0.27}_{-0.13}$. However, this eccentricity would likely result in the instability of the 10 and 16 day planets, in contrast to the stable orbits we find assuming low eccentricities (see Section 8). The too-long duration of planet d only worsens if we assume the $P_d = 8$ day solution. Another resolution of the long-duration transits of planet d is suggested in a contemporaneous paper by Lacedelli et al. (2020): the two apparent transits of planet d might be single-transit events from two distinct planets, each with $P > 16$ days. The similar depths of the transits could result from the observed “peas in a pod” pattern, wherein planets in the same system often have similar sizes (Weiss et al. 2018). We do not detect a secure RV signal at $P > 16$ days that would be consistent with the orbit of either such planet (Section 6). Yet another possibility is that the apparent 2σ tension between the transit duration and orbital period is the result of systematic or random errors in the photometry. Ultimately, additional high-precision photometry is needed to test these various possible explanations for the long durations of planet d. For the rest of this paper, we will assume that the transits are due to a 16 day planet (except where stated otherwise).

5. High-resolution Imaging

As part of our standard process for validating transiting exoplanets to assess the possible contamination of bound or unbound companions on the derived planetary radii (Ciardi et al. 2015) and search for possible sources of astrophysical false positives (e.g., background eclipsing binaries), we obtained high-angular-resolution imaging in the near-infrared and optical.

5.1. Gemini-North and Palomar

We utilized both Gemini-North with NIRI (Hodapp et al. 2003) and Palomar Observatory with PHARO (Hayward et al. 2001) to obtain near-infrared adaptive optics imaging of TOI-561, on 2019 May 24 and 2020 January 8 respectively. Observations were made in the Br γ filter ($\lambda_o = 2.1686$; $\Delta\lambda = 0.0326 \mu\text{m}$). For the Gemini data, 9 dithered images with an exposure time of 2.5 s each were obtained; at Palomar, 15 dithered frames with an exposure of 2.8 s each were obtained. In both cases, the telescope was dithered by a few arcseconds between each exposure, and the dithered science frames were used to create a sky background. Data were reduced using a custom pipeline: we removed bad pixels, performed a sky background subtraction and a flat correction, aligned the stellar position between images, and coadded. The final resolution of the combined dithers was determined from the FWHM of the point-spread function: $0''.13$ and $0''.10$ for the Gemini and Palomar data, respectively.

The sensitivities of the final combined AO images were determined by injecting simulated sources azimuthally around the primary target every 20° at separations of integer multiples of the central source’s FWHM (Furlan et al. 2017). The brightness of each injected source was scaled until standard

aperture photometry detected it with 5σ significance. The resulting brightness of the injected sources relative to the target sets the contrast limits at that injection location. The final 5σ limit at each separation was determined from the average of all of the determined limits at that separation, and the uncertainty on the limit was set by the rms dispersion of the azimuthal slices at a given radial distance.

The sensitivity curves are shown in Figure 7 along with an inset image zoomed to the primary target showing no other companion stars. Both the Gemini and Palomar data reach a $\Delta\text{mag} \approx 2$ at $0''.15$ with an ultimate sensitivity of 7.7 mag and 8.7 mag for the Gemini and Palomar imaging, respectively. To within the limits and sensitivity of the data, no additional companions were detected.

5.2. SOAR and Gemini-South

We also searched for stellar companions with speckle imaging on the 4.1 m Southern Astrophysical Research (SOAR) telescope (Tokovinin et al. 2018) on 2019 May 18 UT. The speckle observations complementing the NIR AO as the *I*-band observations are similar to the TESS bandpass. More details of the observations are available in Ziegler et al. (2020). The observations have a sensitivity of ~ 1 mag at a resolution of $0''.06$ and an ultimate sensitivity of ~ 7 mag at a radius of $3''$. The 5σ detection sensitivity and speckle autocorrelation functions from the observations are shown in Figure 7. As with the NIR AO data, no nearby stars were detected within $3''$ of TOI-561 in the SOAR observations.

High-resolution speckle interferometric images of TOI-561 were obtained on 2020 March 15 UT using the Zorro⁶⁴ instrument mounted on the 8 m Gemini-South telescope located on the summit of Cerro Pachon in Chile. Zorro simultaneously observes in two bands, i.e., 832/40 nm and 562/54 nm, obtaining diffraction-limited images with inner working angles $0''.017$ and $0''.026$, respectively. Our data set consisted of 5 minutes of total integration time taken as sets of 1000×0.06 s images. All the images were combined and subjected to Fourier analysis leading to the production of final data products including speckle reconstructed imagery (see Howell et al. 2011). Figure 7 shows the 5σ contrast curves in both filters for the Zorro observation and includes an inset showing the 832 nm reconstructed image. The speckle imaging results reveal TOI-561 to be a single star to contrast limits of 5 to 8 mag, ruling out main-sequence stars brighter than late M as possible companions to TOI-561 within the spatial limits of ~ 2 to 103 au (at $d = 86$ pc).

6. Radial Velocities

We obtained 60 high-resolution spectra with the W. M. Keck Observatory HIRES instrument on Maunakea, Hawaii between 2019 May and 2020 October, at a cadence of one to two RVs per night. We followed the standard observing and data reduction procedures of the California Planet Search (CPS; Howard et al. 2010). We obtained spectra with the C2 decker, which has dimensions of $14'' \times 0''.86$ and spectral resolution $R \approx 60,000$ at 500 nm. We only observed when the target was at least 25° from the moon. At $V = 10.2$, the star was always at least 8 mag brighter than the moon-illuminated background sky.

⁶³ The custom DV report, which does not use spectroscopic stellar parameters as priors, finds $\rho_* = 0.7 \rho_\odot$, which differs substantially from our spectroscopic determination of $\rho_* = 1.38 \pm 0.11 \rho_\odot$.

⁶⁴ <https://www.gemini.edu/sciops/instruments/alopeke-zorro/>

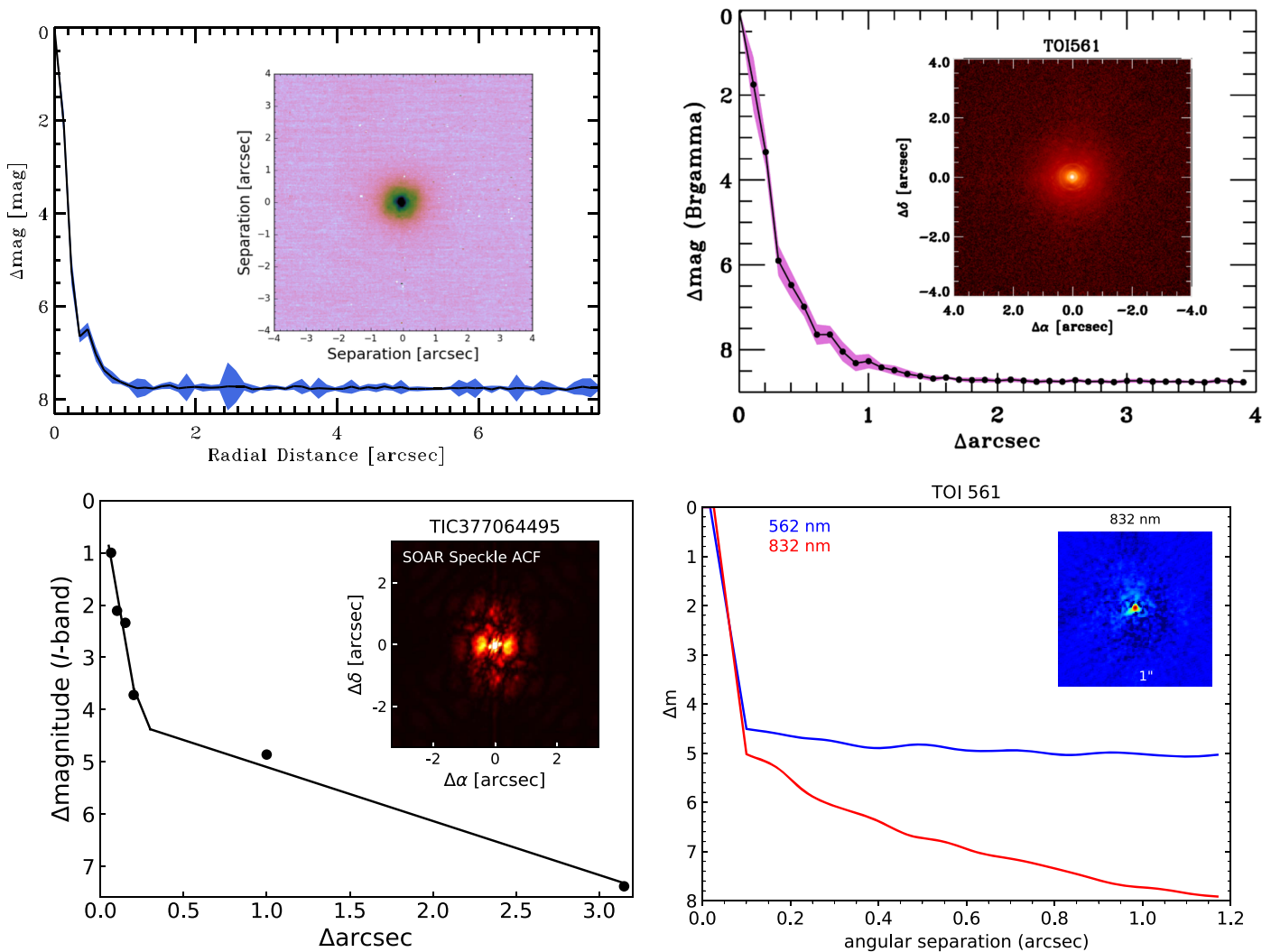


Figure 7. No nearby stars were detected in four independent imaging campaigns. Top left: sensitivity to background stars of our Gemini-N/NIRI images in the Br γ filter. The images were taken in good seeing conditions, and we reach a contrast of 7.5 magnitudes fainter than the host star within $0''.5$. Inset: image of the central portion of the data, centered on the star. Top right: same as top left, but with Palomar. Bottom left: sensitivity to background stars from SOAR speckle imaging observations (5σ upper limits), with an example image inset. Bottom right: same as bottom left, but with Gemini-S/Zorro in two passbands.

We placed a warm cell of molecular iodine gas in the light path as a simultaneous wavelength calibration source for all RV spectra (Marcy & Butler 1992). We obtained a template spectrum by observing the star without the iodine cell. We observed rapidly rotating B stars, with the iodine cell in the light path, immediately before and after the template to model the PSF of the HIRES spectrograph. Each RV spectrum was reproduced with a combination of the deconvolved template spectrum and a laboratory iodine atlas spectrum convolved with the HIRES PSF of the observation (which we empirically determined). The RVs are listed in Table 2 and displayed in Figure 8. Before fitting for any planets, the RVs had an rms of 5.0 m s^{-1} , and the median individual RV error (before applying jitter) was 1.4 m s^{-1} .

When fitting RVs, the mass (and density) determinations of small planets can sensitively depend on the choice of model, particularly the number of planets included and their orbital periods and the use or non-use of correlated-noise models. For example, in the Kepler-10 system, the measured mass of Kepler-10c ranged from 7 to $17 M_{\oplus}$, based on the choice of model (Dumusque et al. 2014; Weiss et al. 2016; Rajpaul et al. 2017). To

test the robustness of our mass and density determinations, we applied several different models to the RVs of TOI-561.

6.1. Three-planet Keplerian Models

We modeled the RVs with the publicly available Python package *radvel* (Fulton et al. 2018). We used the default basis of a five-parameter Keplerian orbit, in which the RV component of each planet is described by its orbital period (P), time of conjunction (T_c), eccentricity (e), the argument of periastron passage (ω), and RV semiamplitude (K). Because the orbital ephemerides from TESS are more precise than what we can constrain with 60 RVs, we fixed P and T_c for each transiting planet at the best-fit values from TESS photometry plus additional ground-based photometry from the TESS Science Group 1.⁶⁵ The eccentricities of all three planets are expected to be small for dynamical reasons. At $P < 1$ day, the USP is almost certainly tidally circularized. The other planets

⁶⁵ We also tried allowing the periods and transit ephemerides to vary but with priors from the best-fit ephemeris, without a substantial difference in the results.

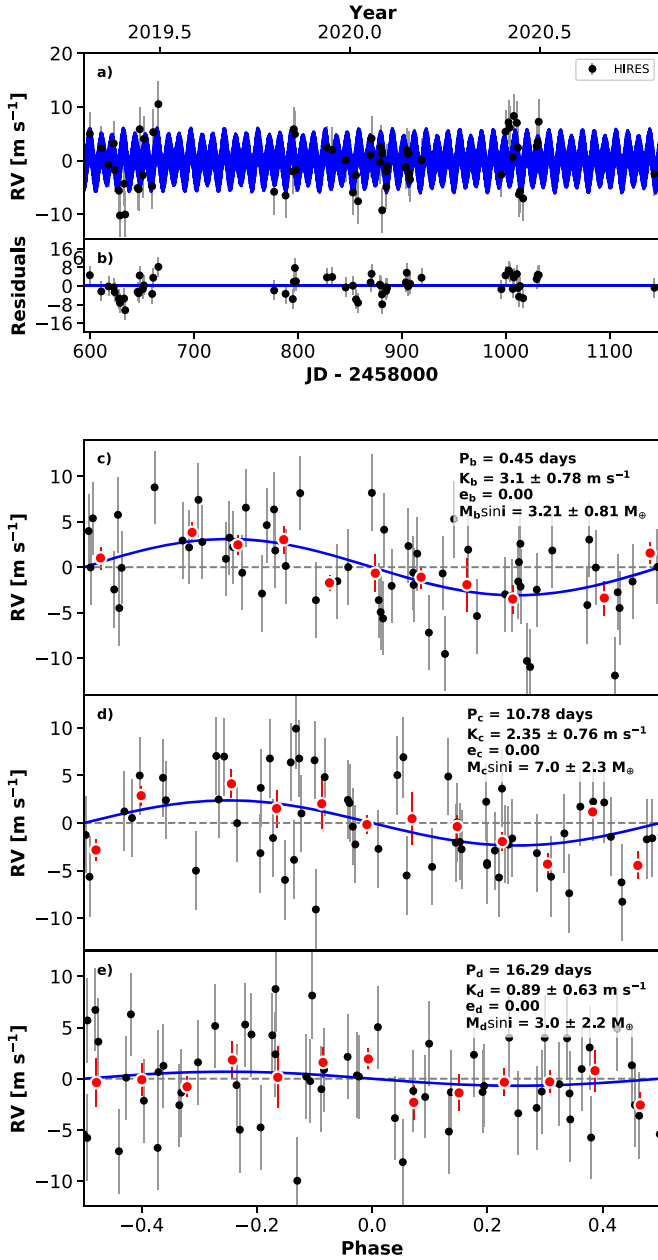


Figure 8. Radial velocities of TOI-561, based on observations from Keck-HIRES (black points). Error bars are 1σ confidence intervals, and the blue line is the best-fit model. The top panel is the full RV time series and residuals. Subsequent panels are the RV components of planets b, c, and d, phase-folded to the orbital period of each planet (the model RV components from the other planets are subtracted from each panel). The red points are RVs binned in phases of 0.1.

have compact orbits ($P_d/P_c \approx 1.5$), such that large eccentricities would result in orbit crossings, and even modest eccentricities would likely result in Lagrange instability (Deck et al. 2013). Furthermore, the majority of small exoplanets in compact configurations have low eccentricities (Mills et al. 2019; Van Eylen et al. 2019). For these reasons, and also because modeling eccentricities introduces two free parameters per planet, we only explored circular fits for all three transiting planets.

Thus, of the five Keplerian parameters that describe each transiting planet, only the semiamplitude (K) was allowed to vary along two global terms: an RV zero-point offset (γ) and an

RV jitter (σ_j), which is added to the individually determined RV errors in quadrature to account for non-Gaussian, correlated noise in the RVs from stellar processes and instrumental systematics. Our full likelihood model was

$$-2 \ln \mathcal{L} = \sum_i \frac{(x_{\text{meas},i} - x_{\text{mod},i})^2}{\sigma_i'^2} + \sum_i \ln(2\pi\sigma_i'^2), \quad (2)$$

where

$$\sigma_i'^2 = \sigma_i^2 + \sigma_j^2 \quad (3)$$

is the quadrature sum of the internal RV error and the jitter.

We optimized the likelihood function with the Powell method (Powell 1964) and used a Markov Chain Monte Carlo (MCMC) analysis⁶⁶ to determine parameter uncertainties. We explored the optimization of several models. In Model A, we did not enforce any priors on planet semiamplitudes (thus allowing values of K , and hence planet mass, to be negative). Although negative planet masses are unphysical, their consideration offsets the bias toward high planet masses that occurs when planet masses are forced to be positive (Weiss & Marcy 2014). The best-fit values with Model A were $K_b = 3.1 \pm 0.8 \text{ m s}^{-1}$, $K_c = 2.2 \pm 0.8 \text{ m s}^{-1}$, and $K_d = 0.3 \pm 0.8 \text{ m s}^{-1}$. The rms of the RV residuals was 4.2 m s^{-1} .

In Model B, we restricted $K > 0$. The advantages of restricting planet masses to be larger than zero are (1) the planet masses are physically motivated, and (2) the residuals are more likely to be useful in searching for additional planets. Model B yielded $K_b = 3.1 \pm 0.8 \text{ m s}^{-1}$, $K_c = 2.4 \pm 0.8 \text{ m s}^{-1}$, and $K_d = 0.9 \pm 0.6 \text{ m s}^{-1}$. The rms of the RV residuals was 4.2 m s^{-1} .

Model C was the same as Model B, except we allowed a linear trend in the RVs, $\dot{\gamma}$, which could be caused by acceleration from a long-period companion. However, the RVs do not strongly favor a trend: $\dot{\gamma} = 0.009 \pm 0.004 \text{ m s}^{-1} \text{ m s}^{-1} \text{ day}^{-1}$, and the best-fit K values changed by less than 1σ with the inclusion of a trend: $K_b = 3.2 \pm 0.8 \text{ m s}^{-1}$, $K_c = 2.1 \pm 0.8 \text{ m s}^{-1}$, and $K_d = 1.0^{+0.7}_{-0.6} \text{ m s}^{-1}$. The rms of the RV residuals was 4.0 m s^{-1} .

In Model D, we considered the hypothesis that planet d has half of the presumed orbital period, which was possible given the gap in the photometry. This model is the same as Model B, except $P_d = 8$ days. This model did not affect the amplitudes of planets b or c, but resulted in $K_d < 2.04 \text{ m s}^{-1}$ (2σ confidence). The rms of the RV residuals was 4.1 m s^{-1} .

In Models A to C, the choice of model makes very little impact on the best-fitting RV semiamplitudes for each planet, and hence our planet mass determinations are robust with respect to our choice of model. For the rest of this paper, we consider Model B as our default model unless stated otherwise. The fitted and fixed parameters of Model B are provided in Table 3.

6.2. Correlated-noise Analysis

The simple Keplerian model fit to observed RVs of TOI-561 displayed an rms of 4.2 m s^{-1} (Figure 8), which is uncharacteristically high for precision RVs of such a bright star (Howard & Fulton 2016). A Lomb-Scargle periodogram of the RV residuals reveals several peaks that might correspond to correlated noise and/or additional planets in the system. However, none of the peaks were significant at the 1%

⁶⁶ Based on emcee, Foreman-Mackey et al. (2013).

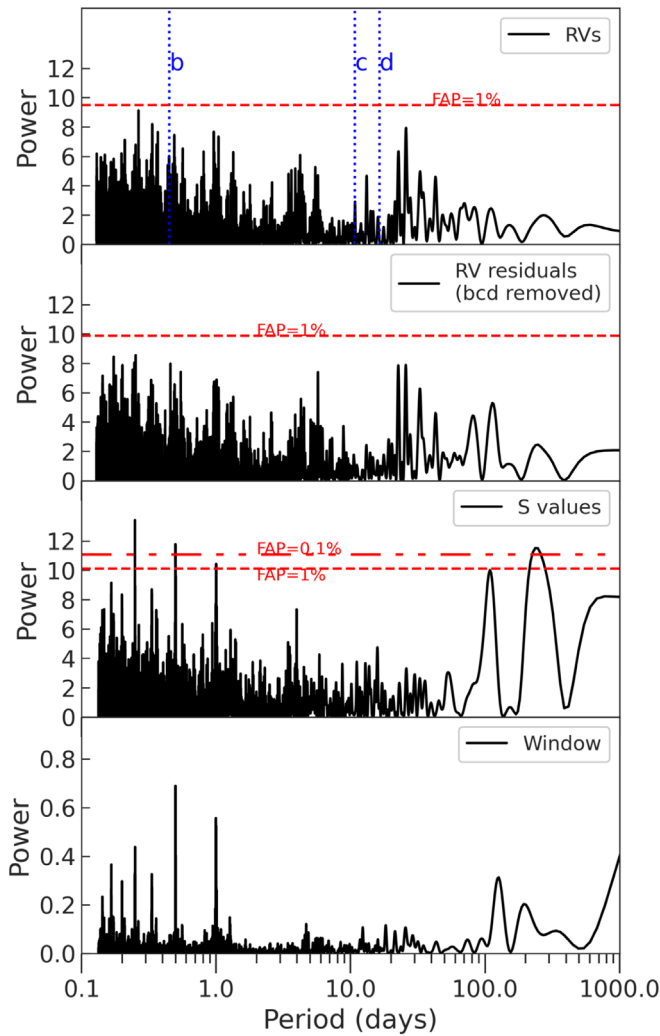


Figure 9. Lomb-Scargle periodograms of (a) the RVs, (b) the RVs after removing the best-fit [Model B] RV signatures from planets b, c, and d, (c) the Mt. Wilson S -value stellar activity indicator time series, and (d) the window function. False-alarm probabilities (FAPs) are computed based on a bootstrap resampling of each time series. The RVs and RV residuals do not have any peaks that cross the 1% FAP. The S values have significant ($\text{FAP} > 1\%$) peaks at 100 days and 230 days, and various short periods that are likely aliases of the longer-period signals caused by the window function.

false-alarm probability (FAP) level, which we determined with bootstrap resampling (Figure 9).

Nonetheless, we considered several correlated-noise models in an attempt to model and remove a putative red-noise component responsible for the high rms of the RV residuals. In Model E, we employed Gaussian process regression (GP), which has been previously applied in analyzing RVs of many exoplanets (e.g., Haywood et al. 2014; Grunblatt et al. 2015). For details of the GP model, see Dai et al. (2017). In principle, the light curve and RVs are both affected by stellar activity rotating in and out of view of the observer (e.g., Aigrain et al. 2012). In an attempt to model the correlated noise in the RVs, we trained the various “hyperparameters” of our GP quasi-periodic kernel using the out-of-transit TESS PDCSAP light curve. We did not detect the stellar rotation period in the TESS PDCSAP or SAP light curves, possibly because the star is very inactive ($\log R'_{\text{HK}} = -5.1$), or the expected rotation period of the star is longer than the photometric baseline. Our MCMC fit to the light curve produced broad posteriors on the rotation

period and the other hyperparameters. Therefore, we did not impose Gaussian priors on the hyperparameters in our GP analysis of the RV data, although we did limit the stellar rotation period < 500 days for quicker convergence. We used EMCEE to constrain the posterior distribution of the GP hyperparameters simultaneously with the orbital parameters of the three planets. We detect the RV signal of planet b: $K_b = 2.9 \pm 0.7 \text{ m s}^{-1}$ and planet c: $K_c = 1.7 \pm 1.0$ and an upper limit for planet d: $K_d < 1.6 \text{ m s}^{-1}$ (95% confidence), all of which are within 1σ of the planet semiamplitudes we determined without the correlated-noise component of the model.

We also attempted to train a correlated-noise model on our spectroscopically determined Mt. Wilson S values. A Lomb-Scargle periodogram of the S values shows two significant peaks: one at 100 days and the other at 230 days, both of which cross the 1% FAP threshold (which we computed with bootstrap resampling, Figure 9). (The forest of regular peaks with $P < 1$ day are likely aliases produced by our window function, which had poor sampling below 1 day). Note that these periods differ from the most prominent peaks in the RV residuals, which are a doublet near 25 days. Furthermore, the S values are not sampled as frequently as the light curve, but they are sampled simultaneously with the RVs, and they are a direct indicator of the chromospheric magnetic activity during the observations. We tried a GP with a quasi-periodic kernel trained on the S values (Model F), but this did not produce significant changes in the semiamplitudes of the planets or the rms of the RV residuals, possibly because the S values had small variability or were sparsely sampled. We also tried a model in which we decorrelated the RVs with respect to the S values (Model G), which did not reduce the rms (and thus did not remove the correlated noise).

None of our attempts to model correlated noise in the RVs changed the amplitudes of the planets or reduced the rms of the RV residuals, and so we prefer the simpler Keplerian models (without correlated noise) described above. Perhaps TOI-561 is too inactive for models trained on stellar activity to be effective, given the current quality of the data. For comparison, Kepler-10, another system with time-correlated RV residuals, has $\log R'_{\text{HK}} = -4.89$, which is more active than TOI-561 $\log R'_{\text{HK}} = -5.1$. The use of GPs affected the mass determination of Kepler-10 c, lowering it from $14 M_{\oplus}$ (no GP) to $7 M_{\oplus}$ (with GP). Perhaps there is a minimum stellar activity for which attempts to decorrelate the stellar activity signal can be successful, given RVs with precision of 2 m s^{-1} .

Nonetheless, there are substantial correlated residuals in the RVs of TOI-561 which are uncharacteristic of the HIRES instrument performance (typically 2 m s^{-1} for $V < 11$; Howard & Fulton 2016). The residual RVs of TOI-561 are not well explained by any of our models of stellar activity, and so perhaps additional planets contribute to the RV residuals. More RVs are needed to identify the orbital periods of any such planets and model their Keplerian signals.

7. Planet Masses and Densities

Each K value can be converted to the planet’s minimum mass, $M_p \sin i$, but because all three planets transit, actual masses (rather than minimum masses) can be calculated. Assuming Model B, we find $M_b = 3.2 \pm 0.8 M_{\oplus}$, $M_c = 7.0 \pm 2.3 M_{\oplus}$, and $M_d = 3.0^{+2.4}_{-1.9} M_{\oplus}$. Furthermore, because the planets transit, their radii are calculated from the planet-to-star radius ratios

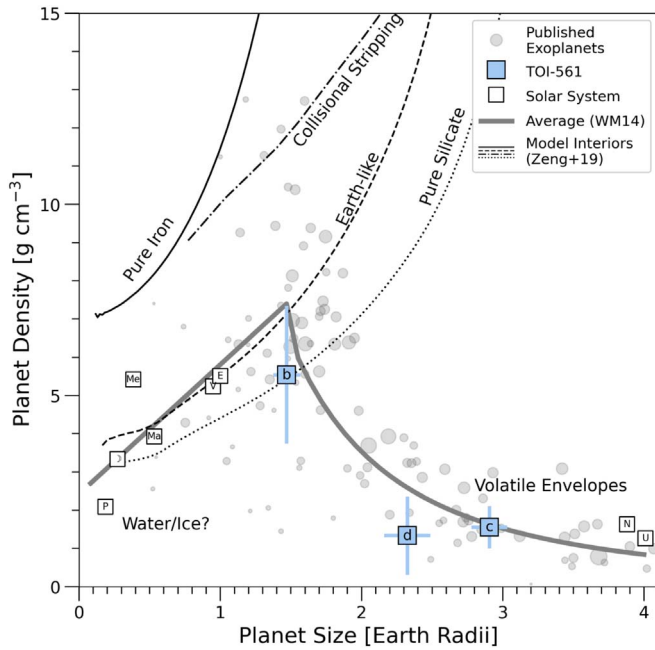


Figure 10. Planet bulk density vs. planet radius for small planets with measured radii ($R_p < 4 R_\oplus$, $\sigma(R_p)/R_p < 0.2$) and masses ($\sigma(M_p) < 2 M_\oplus$), based on results from the NASA Exoplanet Archive (queried 2020 June 24 by Akeson et al. 2013, gray points). The point size is scaled to $\rho_p/\sigma(\rho_p)$. The Weiss & Marcy (2014) average mass–radius relationship, several model composition curves from Zeng et al. (2019), and the theoretical maximum density from collisional stripping (Marcus et al. 2010) are shown. The solar system planets and Earth’s moon are provided for context. The TOI-561 planets are consistent with or slightly less dense than typical planets of their sizes. TOI-561 b is 1σ less dense than an Earth-composition planet.

and known stellar radius: $R_b = 1.45 \pm 0.11 R_\oplus$, $R_c = 2.90 \pm 0.13 R_\oplus$, and $R_d = 2.32 \pm 0.16 R_\oplus$. The bulk densities of the planets are $\rho_b = 5.5^{+2.0}_{-1.6} \text{ g cm}^{-3}$, $\rho_c = 1.6 \pm 0.6 \text{ g cm}^{-3}$, and $\rho_d = 1.3^{+1.1}_{-0.8} \text{ g cm}^{-3}$. The derived physical and orbital properties of the planets are summarized in Table 3.

The masses and densities of the TOI-561 planets are shown in comparison to the masses and densities of other sub-Neptune-size planets in Figure 10. The other planet masses and densities come from the NASA Exoplanet Archive, from which we included only those with $\sigma(M_p) < 2 M_\oplus$.

7.1. TOI-561 b

The USP TOI-561 b has a typical mass and density for its size. At $1.5 R_\oplus$ and $5.5^{+2.0}_{-1.6} \text{ g cm}^{-3}$, it is 1σ below the peak of the density–radius diagram identified in Weiss & Marcy (2014), consistent with a rocky composition that is either Earth like or iron poor. Nearly all USPs are smaller than $2 R_\oplus$ and are expected to have rocky compositions, given their small sizes and extreme stellar irradiation (Sanchis-Ojeda et al. 2015), and TOI-561 b is consistent with this expectation. In a homogeneous analysis of USPs with masses determined from RVs, Dai et al. (2019) found that most USPs with $< 10 M_\oplus$ are consistent with having Earth-like compositions, whereas the few USPs with $> 10 M_\oplus$ likely have H/He envelopes. TOI-561 b ($3.2 \pm 0.8 M_\oplus$) is consistent with the rocky group of that study.

The minimum density of a USP can be determined from its orbital period and the requirement that it orbits outside the Roche limiting distance (Rappaport et al. 2013). We investigated the minimum density of TOI-561 b, with the hope that it

would provide additional constraints on the mass of the planet. Using the approximation from Sanchis-Ojeda et al. (2014), we find that the minimum density of the USP is

$$\rho_p [\text{g cm}^{-3}] \geq (11.3 \text{ hr}/P_{\text{orb}})^2 = 1.15 \text{ g cm}^{-3} \quad (4)$$

for TOI-561 b, which is below our measured density and corresponds to a minimum mass of $0.64 M_\oplus$. Such a low mass is ruled out by the data at nearly 3σ confidence. Thus, TOI-561 b is not close enough to its star for the Roche stability criterion to provide additional information about the density.

An interpretation of the USP composition that involves a H/He layer is disfavored by physical models. At a sufficiently low stellar irradiation level, the low density of TOI-561 b might have been consistent with a composition of an Earth-like core overlaid with a thin H/He envelope. However, at $P = 0.44$ days (with equilibrium temperature $> 2000 \text{ K}$) and a mass of $\sim 3 M_\oplus$, the USP is too irradiated and too low mass to hold onto a H/He envelope (Lopez 2017).

7.2. TOI-561 c and d

At $R_p > 1.5 R_\oplus$ and with low densities, TOI-561 c and d have substantial gaseous envelopes by volume, although the gas envelopes likely only constitute $\sim 1\%$ of the planet masses (Lopez & Fortney 2014). TOI-561 c has a radius and mass consistent with the Weiss & Marcy (2014) empirical mass–radius relationship.

The ambiguity of the orbital period for planet d poses a challenge to accurate mass determination. Our RVs are consistent with a nondetection of planet d at both the $P_d = 16$ and $P_d = 8$ day orbits. Assuming $P_d = 16$ days, the RVs provide an upper limit of $K_d < 2.1 \text{ m s}^{-1}$, which corresponds to $M_p < 7.0 M_\oplus$ (2σ confidence; see Section 6). Assuming $P_d = 8$ days, the RVs provide an upper limit of $K < 2.0 \text{ m s}^{-1}$, which corresponds to $M_p < 5.6 M_\oplus$ (2σ confidence). In either scenario, the mass of TOI-561 d is approximately 2σ below the Weiss & Marcy (2014) mass–radius relationship and is too low to be consistent with a rocky composition, given the planet’s radius. However, if planet d is actually the transits of two distinct planets as suggested in Lacedelli et al. (2020), the low mass presented here does not apply.

7.3. Nondetection of Outer Giant Planets

With our 1.5 year baseline of RVs, we were able to place constraints on possible long-period giant planets. In Model C, we found a 3σ upper limit to an RV trend of $\dot{\gamma} < 0.02 \text{ m s}^{-1} \text{ day}^{-1}$. This observational limit on the acceleration of the star can be converted to a limit on the mass and orbital distance of a possible perturber by setting it equal to the gravitational acceleration from a planet at distance r : $GM_\star M_p r^{-2} = M_\star \dot{\gamma}$, where G is the gravitational constant and r is the distance between the perturber and the star at the time the RVs were measured. Assuming a circular orbit for the putative giant planet ($r = a$), we find

$$\frac{M_p \sin i}{M_J} \left(\frac{a}{5 \text{ au}} \right)^{-2} < 1.0 \quad (5)$$

(3σ confidence). Thus, our nondetection of an RV acceleration rules out a $1.0 M_J$ planet at 5 au with 3σ confidence (assuming $\sin i \approx 1$, $e = 0$, and that we did not primarily sample the orbit while the planet was moving parallel to the sky plane). In systems with compact configurations of transiting planets, giant

planets often need to be approximately coplanar with the transiting planets in order for the inner planets to remain mutually continuously transiting (Becker & Adams 2017), and so we do not expect nontransiting companions to have face-on orbits. Thus, the nondetection of an RV trend rules out a variety of scenarios of a coplanar giant planet near the snow line.

8. Discussion

8.1. Stability

We investigated whether we could constrain the architecture of the TOI-561 system and in particular the orbital period of planet d, with stability arguments. To assess stability, we used *Spock*, a machine-learning-based approach to inferring orbital stability (Tamayo et al. 2020). *Spock* incorporates several analytic indicators (including MEGNO, AMD, and mutual Hill radius) with an N -body integration of 10^4 orbits to compute a probabilistic assessment of the system stability. We tested the architectures of TOI-561 with planet d at $P_d = 16$ days (Model B) and at $P_d = 8$ days (Model D). Because stability depends sensitively on the eccentricities and inclinations of planets in compact configurations, we varied the eccentricities, arguments of periastron passage, and inclinations. The eccentricities and inclinations in multiplanet systems are well fit with Rayleigh distributions with characteristic values $\sigma_e = 0.035$ and $\sigma_i = 2.45^\circ$ (Mills et al. 2019), and so we sampled 1000 trials from these distributions (sampling ω uniformly on $[0, \pi]$). For Model B, the probability of stability is $95\% \pm 3\%$, whereas for Model D, the probability of stability is $84\% \pm 30\%$. Thus, although more configurations of Model B are stable, we cannot rule out Model D based on a stability argument.

8.2. Formation and Evolution

TOI-561 is the second transiting multiplanet system discovered around a galactic thick-disk star (Kepler-444, Campante et al. 2015, is the first), and is the first galactic thick-disk star with a USP. The iron-poor, α -enhanced stellar abundances observed today are likely representative of the nebular environment in which the planets formed. Thus, TOI-561 provides an opportunity to study the outcome of planet formation in an environment that is chemically distinct from most of the planetary systems known to date. Furthermore, its membership in the galactic thick disk indicates old age, making the rocky planet TOI-561 b one of the oldest rocky planets known.

The confirmed old age of the system is relevant for dynamical studies of the planets. For instance, the formation of USPs is still poorly understood. The majority of USPs are the only detected transiting planet in their systems (Sanchis-Ojeda et al. 2014). This is partially due to a bias of geometry (as planet detection probability scales with R_*/a). However, Dai et al. (2018) found that the mutual inclinations in multiplanet systems with USPs are significantly larger than those in multiplanet systems without USPs, suggesting that systems with USPs have had more dynamically “hot” histories. One mechanism for generating large mutual inclinations in systems with USPs is if the host star is oblate and misaligned with respect to the planets (Li et al. 2020).

Furthermore, dynamical interactions in a multiplanet system can move short-period planets to ultra-short periods in a manner that may excite large eccentricities. Petrovich et al. (2019) proposed a mechanism of secular chaos in which the

innermost planet is kicked to a high-eccentricity orbit, which is then circularized. In contrast, Pu & Lai (2019) proposed a scheme in which the innermost planet’s neighbors consistently force it to a low-eccentricity orbit, which results in inward migration and eventual circularization.

In a study of the Gaia-DR2 kinematics of USP host stars in the Kepler field, Hamer & Schlaufman (2020) found that their motions are similar to those of matched field stars (rather than young stars). The broad range of ages of USPs suggests that USPs do not undergo rapid tidal inspiral during the host star’s main-sequence lifetime. The existence of a USP around an 10 Gyr old star is consistent with this finding.

8.3. Predicted Transit Timing Variations

Because planets c and d have an orbital period ratio of ~ 1.5 or less, the planets likely perturb each other’s orbits, producing transit timing variations (TTVs). The TESS sector 8 baseline was too short to detect TTVs (only two transits of each planet were detected). The approximate amplitude of the TTV signal can be computed analytically using the expressions from Lithwick et al. (2012):

$$|V| \approx P\mu'/\Delta + \mathcal{O}(e)/\Delta, \quad (6)$$

where P is the orbital period of the inner planet, μ' is the mass of the perturbing, outer planet (in units of stellar mass), $\mathcal{O}(e)$ is a first-order dependency on the free eccentricities of the planets, and Δ is the nondimensional distance from mean motion resonance:

$$\Delta = \frac{P'}{P} \frac{j-1}{j} - 1, \quad (7)$$

where P and P' are the inner and outer orbital periods and j is an integer. Equation (6) can be used to approximate the TTV amplitude of the outer planet by setting $P \rightarrow P'$ and $\mu' \rightarrow \mu$ (for a thorough derivation and caveats, see Lithwick et al. 2012).

Using the values for the planet masses determined in Section 7 and assuming circular orbits, we find that the TTV amplitude of planet c ($P = 10.78$ days) is about 6 minutes, whereas the TTV amplitude of planet d is either 30 minutes (if $P_d = 16$ days; $j = 3$) or 15 minutes (if $P_d = 8.14$ days, $j = 4$).

8.4. Atmospheric Probing Metrics

Using the system parameters tabulated in this paper, we calculated the transmission and emission spectroscopy metrics (TSM and ESM, respectively) of Kempton et al. (2018) to determine whether these newly characterized planets are compelling targets for future atmospheric or surface characterization via transit or eclipse spectroscopy. Assuming a flat prior on the planets’ Bond albedos from 0 to 0.4 and on their efficiency of day-to-night energy recirculation from $1/4$ to $2/3$, and propagating the uncertainties on all relevant parameters, we calculate the planets’ equilibrium temperatures to be 2480 ± 200 K, 860 ± 70 K, and 750 ± 60 K for planets b, c, and d, respectively. Because of the relatively shallow transit depths ($\lesssim 1000$ ppm for all three planets), space-based spectroscopy is likely to be the only feasible avenue for such studies. In contrast to some recent reports of these quantities for other newly discovered TESS planets, here we propagate all parameter uncertainties in order to report how well the TSM and ESM are constrained, as well as how promising the median

Table 4
Atmospheric Prospects

Planet	TSM	ESM	Notes
b	11^{+73}_{-4}	8.7 ± 1.1	Good eclipse target
c	93^{+55}_{-37}	4.87 ± 0.39	Promising transmission target
d ^a	82^{+109}_{-33}	2.15 ± 0.29	Promising transmission target

Note.

^a Assuming $P_d = 16$ days. If $P_d = 8$ days then $TSM_d = 103^{+137}_{-43}$ (68% confidence interval).

values are; this is especially essential when planetary properties are not yet measured to high precision. We report the transmission and emission metrics and their uncertainties in Table 4.

Our analysis shows that TOI-561 b is among the best TESS targets discovered to date for thermal emission measurements (see Table 3 of Astudillo-Defru et al. 2020). With $ESM = 7.1 \pm 1.1$, planet b is clearly a promising target for observations of its secondary eclipse and/or its full-orbit phase curves, as has previously been done for other irradiated terrestrial planets such as 55 Cnc e (Demory et al. 2012, 2016) and LHS 3844b (Kreidberg et al. 2019). The uncertainty on planet b’s ESM is dominated by the uncertainty on its transit depth, but regardless, the planet has a reliably high metric in this category. Because of their cooler temperatures, the lower ESM values for planets b and c mark them as less attractive targets for secondary eclipse studies.

As for transit spectroscopy, the TSM values for the sub-Neptunes TOI-561 c and d listed in Table 4 (93^{+55}_{-37} and 82^{+109}_{-33} , respectively) indicate that they may be particularly amenable to transmission studies. However, because the TSM scales inversely with planetary surface gravity, this result depends on determining more precise values of these planets’ masses. These planets clearly warrant additional precise RV follow-up: if the expectation values of their TSMs do not change as the uncertainties shrink, these two planets would be among the top 20 confirmed warm Neptunes for transmission spectroscopy (see Table 11 of Guo et al. 2020). Due to the small size of the highly irradiated planet b, and because it is unlikely to have retained much of an atmosphere, it is not an appealing target for transmission measurements.

Better ephemerides for planets c and d are necessary in preparation for atmospheric studies. The alias of the orbit of planet d should be resolved prior to interpretation of the planetary atmospheres, as the factor of 2 change in the orbital period produces a factor of ~ 1.3 change in the equilibrium temperature. Also, planet d may have significant TTVs with amplitudes of ~ 30 minutes (assuming the orbital period is 16 days).

9. Conclusion

TOI-561 is a system with multiple transiting planets identified by the NASA TESS spacecraft. In this paper, we have confirmed two of the planets, including a rocky USP, with ground-based follow-up, and also characterized the properties of the planet and the host star. We found:

1. TOI-561 is a metal-poor, α -enhanced member of the galactic thick disk ($[Fe/H] = -0.4$, $\alpha = 0.2$). It is one of the oldest planetary systems yet identified and one of the most metal poor. In both of these aspects, it is an

important benchmark in our understanding of planet formation and evolution.

2. We confirm the planets b (TOI-561.02, $P_b = 0.45$ days, $R_b = 1.45 \pm 0.11 R_\oplus$) and c (TOI-561.01, $P_c = 10.78$ days, $R_c = 2.90 \pm 0.13 R_\oplus$) with RVs, high-resolution imaging, and ground-based photometry. We rule out a variety of astrophysical false positives for planet d (TOI-561.03, $P_d = 16.29$ days, $R_d = 2.32 \pm 0.16 R_\oplus$) but note that the ephemeris is highly uncertain.
3. With 60 RVs from Keck-HIRES, we determined the mass and density of the USP rocky planet TOI-561 b: $M_b = 3.2 \pm 0.8 M_\oplus$, $\rho_b = 5.5^{+2.0}_{-1.6} \text{ g cm}^{-3}$. Planet b has a below-average density for its size (by 1σ), suggesting an iron-poor composition in the core.
4. We also determined the mass and density of planet c ($M_c = 7.0 \pm 2.3 M_\oplus$, $\rho_c = 1.6 \pm 0.6 \text{ g cm}^{-3}$) and an upper limit for the mass of planet d assuming $P_d = 16$ days ($M_d = 3.0^{+2.4}_{-1.9} M_\oplus$). The large radii and low masses of planets c and d are consistent with thick volatile envelopes overlying rocky cores.
5. The RVs from Keck-HIRES span 1.5 years and do not have a significant trend. The nondetection of a trend rules out various scenarios of a giant planet near the ice line.
6. Thanks to the bright host star, this multiplanet system is amenable to atmospheric follow-up with space-based telescopes. Planet b is expected to be a good eclipse target, while planets c and d are promising targets for transmission spectroscopy. Comparative atmospheric properties for the planets in this very metal-poor system would provide a unique test for planet formation scenarios.

We thank the time assignment committees of the University of California, the California Institute of Technology, NASA, and the University of Hawaii for supporting the TESS-Keck Survey with observing time at the W. M. Keck Observatory and on the Automated Planet Finder.

We thank NASA for funding associated with our NASA-Keck Key Strategic Mission Support project. We gratefully acknowledge the efforts and dedication of the Keck Observatory staff for support of HIRES and remote observing. We recognize and acknowledge the cultural role and reverence that the summit of Maunakea has within the indigenous Hawaiian community. We are deeply grateful to have the opportunity to conduct observations from this mountain.

We thank Ken and Gloria Levy, who supported the construction of the Levy Spectrometer on the Automated Planet Finder. We thank the University of California and Google for supporting Lick Observatory and the UCO staff for their dedicated work scheduling and operating the telescopes of Lick Observatory. This paper is based on data collected by the TESS mission. Funding for the TESS mission is provided by the NASA Explorer Program. We acknowledge the use of public TESS Alert data from pipelines at the TESS Science Office and at the TESS Science Processing Operations Center. We thank David Latham for organizing the TESS community follow-up program, which brought together the widespread authorship and diversity of resources presented in this manuscript.

The work includes observations obtained at the international Gemini Observatory, a program of NSF’s NOIRLab acquired through the Gemini Observatory Archive at NSF’s NOIRLab,

which is managed by the Association of Universities for Research in Astronomy (AURA) under a cooperative agreement with the National Science Foundation on behalf of the Gemini Observatory partnership: the National Science Foundation (United States), National Research Council (Canada), Agencia Nacional de Investigación y Desarrollo (Chile), Ministerio de Ciencia, Tecnología e Innovación (Argentina), Ministério da Ciência, Tecnologia, Inovações e Comunicações (Brazil), and Korea Astronomy and Space Science Institute (Republic of Korea). Data were collected under program GN-2019A-LP-101. Observations in the paper made use of the High-Resolution Imaging instrument Zorro. Zorro was funded by the NASA Exoplanet Exploration Program and built at the NASA Ames Research Center by Steve B. Howell, Nic Scott, Elliott P. Horch, and Emmett Quigley. Zorro was mounted on the Gemini-South telescope of the international Gemini Observatory. Observations also made use of the NIRI instrument, which is mounted at Gemini-North. The Gemini-North telescope is located within the Maunakea Science Reserve and adjacent to the summit of Maunakea. We are grateful for the privilege of observing the universe from a place that is unique in both its astronomical quality and its cultural significance.

This work makes use of observations from the LCOGT network. This article is based on observations made with the MuSCAT2 instrument, developed by ABC, at Telescopio Carlos Sánchez operated on the island of Tenerife by the IAC in the Spanish Observatorio del Teide. This work is partly supported by JSPS KAKENHI grant Nos. JP17H04574, JP18H01265, and JP18H05439, and JST PRESTO grant No. JPMJPR1775. This work makes use of data collected under the NGTS project at the ESO La Silla Paranal Observatory. The NGTS facility is operated by the consortium institutes with support from the UK Science and Technology Facilities Council (STFC) projects ST/M001962/1 and ST/S002642/1.

This work has made use of data from the European Space Agency (ESA) mission Gaia (<https://www.cosmos.esa.int/gaia>), processed by the Gaia Data Processing and Analysis Consortium (DPAC, <https://www.cosmos.esa.int/web/gaia/dpac/consortium>). Funding for the DPAC has been provided by national institutions, in particular the institutions participating in the Gaia Multilateral Agreement. J.S.J. acknowledges support by FONDECYT grant 1201371, and partial support from CONICYT project Basal AFB-170002. J.I.V. acknowledges support of CONICYT-PFCHA/Doctorado Nacional-21191829.

This research has made use of the Exoplanet Follow-up Observing Program (ExoFOP), which is operated by the California Institute of Technology, under contract with the National Aeronautics and Space Administration. Resources supporting this work were provided by the NASA High-End Computing (HEC) Program through the NASA Advanced Supercomputing (NAS) Division at Ames Research Center for the production of the SPOC data products.

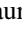
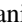
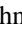


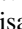

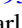
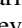

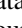
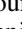
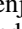
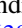







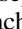
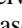




L.M.W. is supported by the Beatrice Watson Parrent Fellowship and NASA ADAP Grant 80NSSC19K0597. D.H. acknowledges support from the Alfred P. Sloan Foundation, the National Aeronautics and Space Administration (80NSSC18K1585, 80NSSC19K0379), and the National Science Foundation (AST-1717000). E.A.P. acknowledges the support of the Alfred P. Sloan Foundation. C.D.D. acknowledges the support of the Hellman Family Faculty Fund, the Alfred P. Sloan Foundation, the David

& Lucile Packard Foundation, and the National Aeronautics and Space Administration via the TESS Guest Investigator Program (80NSSC18K1583). I.J.M.C. acknowledges support from the NSF through grant AST-1824644. Z.R.C. acknowledges support from the TESS Guest Investigator Program (80NSSC18K18584). A.C. acknowledges support from the National Science Foundation through the Graduate Research Fellowship Program (DGE 1842402). P.D. acknowledges support from a National Science Foundation Astronomy and Astrophysics Postdoctoral Fellowship under award AST-1903811. A.B. is supported by the NSF Graduate Research Fellowship, grant No. DGE 1745301. R.A.R. is supported by the NSF Graduate Research Fellowship, grant No. DGE 1745301. M.R.K. is supported by the NSF Graduate Research Fellowship, grant No. DGE 1339067. J.N.W. thanks the Heising Simons Foundation for support.

Facilities: TESS, Keck I-HIRES, Gemini-North-NIRI, Gemini-South-Zorro, Palomar, SOAR, LCOGT, NGTS, El Sauce, PEST, MuSCAT2.

Software: Astropy (Astropy Collaboration et al. 2013, 2018), radvel (Fulton et al. 2018), emcee (Foreman-Mackey et al. 2013), Spectroscopy Made Easy (Valenti & Piskunov 1996; Piskunov & Valenti 2017), SpecMatch Synth (Petigura 2015), SpecMatch-Emp (Yee et al. 2017), isoclassify (Huber et al. 2017), AstroImageJ (Collins et al. 2017), lightkurve (Lightcurve Collaboration et al. 2018), spock (Tamayo et al. 2020), kiahoku (Claytor et al. 2020).

ORCID iDs

Lauren M. Weiss  <https://orcid.org/0000-0002-3725-3058>
 Fei Dai  <https://orcid.org/0000-0002-8958-0683>
 Daniel Huber  <https://orcid.org/0000-0001-8832-4488>
 John M. Brewer  <https://orcid.org/0000-0002-9873-1471>
 Karen A. Collins  <https://orcid.org/0000-0001-6588-9574>
 David R. Ciardi  <https://orcid.org/0000-0002-5741-3047>
 Elisabeth C. Matthews  <https://orcid.org/0000-0003-0593-1560>
 Carl Ziegler  <https://orcid.org/0000-0002-0619-7639>
 Steve B. Howell  <https://orcid.org/0000-0002-2532-2853>
 Natalie M. Batalha  <https://orcid.org/0000-0002-7030-9519>
 Courtney Dressing  <https://orcid.org/0000-0001-8189-0233>
 Benjamin Fulton  <https://orcid.org/0000-0003-3504-5316>
 Andrew W. Howard  <https://orcid.org/0000-0001-8638-0320>
 Howard Isaacson  <https://orcid.org/0000-0002-0531-1073>
 Stephen R. Kane  <https://orcid.org/0000-0002-7084-0529>
 Erik A. Petigura  <https://orcid.org/0000-0003-0967-2893>
 Paul Robertson  <https://orcid.org/0000-0003-0149-9678>
 Arpita Roy  <https://orcid.org/0000-0001-8127-5775>
 Ryan A. Rubenzahl  <https://orcid.org/0000-0003-3856-3143>
 Joseph D. Twicken  <https://orcid.org/0000-0002-6778-7552>
 Zachary R. Claytor  <https://orcid.org/0000-0002-9879-3904>
 Keivan G. Stassun  <https://orcid.org/0000-0002-3481-9052>
 Mason G. MacDougall  <https://orcid.org/0000-0003-2562-9043>
 Ashley Chontos  <https://orcid.org/0000-0003-1125-2564>
 Steven Giacalone  <https://orcid.org/0000-0002-8965-3969>
 Paul A. Dalba  <https://orcid.org/0000-0002-4297-5506>
 Teo Mocnik  <https://orcid.org/0000-0003-4603-556X>
 Michelle L. Hill  <https://orcid.org/0000-0002-0139-4756>
 Corey Beard  <https://orcid.org/0000-0001-7708-2364>
 Joseph M. Akana Murphy  <https://orcid.org/0000-0001-8898-8284>

Lee J. Rosenthal  <https://orcid.org/0000-0001-8391-5182>
 Aida Behmard  <https://orcid.org/0000-0003-0012-9093>
 Judah Van Zandt  <https://orcid.org/0000-0002-4290-6826>
 Jack Lubin  <https://orcid.org/0000-0001-8342-7736>
 Molly R. Kosiarek  <https://orcid.org/0000-0002-6115-4359>
 Michael B. Lund  <https://orcid.org/0000-0003-2527-1598>
 Jessie L. Christiansen  <https://orcid.org/0000-0002-8035-4778>
 Rachel A. Matson  <https://orcid.org/0000-0001-7233-7508>
 Joshua E. Schlieder  <https://orcid.org/0000-0001-5347-7062>
 Erica J. Gonzales  <https://orcid.org/0000-0002-9329-2190>
 César Briceño  <https://orcid.org/0000-0001-7124-4094>
 Nicholas Law  <https://orcid.org/0000-0001-9380-6457>
 Andrew W. Mann  <https://orcid.org/0000-0003-3654-1602>
 Kevin I. Collins  <https://orcid.org/0000-0003-2781-3207>
 Phil Evans  <https://orcid.org/0000-0002-5674-2404>
 Akihiko Fukui  <https://orcid.org/0000-0002-4909-5763>
 Eric L. N. Jensen  <https://orcid.org/0000-0002-4625-7333>
 Felipe Murgas  <https://orcid.org/0000-0001-9087-1245>
 Norio Narita  <https://orcid.org/0000-0001-8511-2981>
 Enric Palle  <https://orcid.org/0000-0003-0987-1593>
 Hannu Parviainen  <https://orcid.org/0000-0001-5519-1391>
 Richard P. Schwarz  <https://orcid.org/0000-0001-8227-1020>
 Thiam-Guan Tan  <https://orcid.org/0000-0001-5603-6895>
 Jack S. Acton  <https://orcid.org/0000-0002-1860-7842>
 Edward M. Bryant  <https://orcid.org/0000-0001-7904-4441>
 Alexander Chaushev  <https://orcid.org/0000-0003-0061-5446>
 Sam Gill  <https://orcid.org/0000-0002-4259-0155>
 Philipp Eigmüller  <https://orcid.org/0000-0003-4096-0594>
 Jon Jenkins  <https://orcid.org/0000-0002-4715-9460>
 George Ricker  <https://orcid.org/0000-0003-2058-6662>
 Sara Seager  <https://orcid.org/0000-0002-6892-6948>
 Joshua N. Winn  <https://orcid.org/0000-0002-4265-047X>

References

- Abadi, M. G., Navarro, J. F., Steinmetz, M., & Eke, V. R. 2003, *ApJ*, **591**, 499
 Adibekyan, V. Z., Sousa, S. G., Santos, N. C., et al. 2012, *A&A*, **545**, A32
 Aigrain, S., Pont, F., & Zucker, S. 2012, *MNRAS*, **419**, 3147
 Akeson, R. L., Chen, X., Ciardi, D., et al. 2013, *PASP*, **125**, 989
 Astropy Collaboration, Price-Whelan, A. M., Sipőcz, B. M., et al. 2018, *AJ*, **156**, 123
 Astropy Collaboration, Robitaille, T. P., Tollerud, E. J., et al. 2013, *A&A*, **558**, A33
 Astudillo-Defru, N., Cloutier, R., Wang, S. X., et al. 2020, *A&A*, **636**, A58
 Barbary, K. 2016, *JOSS*, **1**, 58
 Becker, J. C., & Adams, F. C. 2017, *MNRAS*, **468**, 549
 Bensby, T., Feltzing, S., & Lundström, I. 2004, *A&A*, **415**, 155
 Bensby, T., Feltzing, S., Lundström, I., & Ilyin, I. 2005, *A&A*, **433**, 185
 Bensby, T., Feltzing, S., & Oey, M. S. 2014, *A&A*, **562**, A71
 Bertin, E., & Arnouts, S. 1996, *A&AS*, **117**, 393
 Borucki, W. J., Koch, D., Basri, G., et al. 2010, *Sci*, **327**, 977
 Bovy, J., Rix, H.-W., & Hogg, D. W. 2012, *ApJ*, **751**, 131
 Brewer, J. M., Fischer, D. A., Basu, S., Valenti, J. A., & Piskunov, N. 2015, *ApJ*, **805**, 126
 Brewer, J. M., Fischer, D. A., Valenti, J. A., & Piskunov, N. 2016, *ApJS*, **225**, 32
 Brook, C. B., Kawata, D., Gibson, B. K., & Freeman, K. C. 2004, *ApJ*, **612**, 894
 Brown, T. M., Baliber, N., Bianco, F. B., et al. 2013, *PASP*, **125**, 1031
 Bryant, E. M., Bayliss, D., McCormac, J., et al. 2020, *MNRAS*, **494**, 5872
 Buchhave, L. A., Latham, D. W., Johansen, A., et al. 2012, *Natur*, **486**, 375
 Campante, T. L., Barclay, T., Swift, J. J., et al. 2015, *ApJ*, **799**, 170
 Carrillo, A., Hawkins, K., Bowler, B. P., Cochran, W., & Vanderburg, A. 2020, *MNRAS*, **491**, 4365
 Casagrande, L., Ramírez, I., Meléndez, J., Bessell, M., & Asplund, M. 2010, *A&A*, **512**, A54
 Choi, J., Dotter, A., Conroy, C., et al. 2016, *ApJ*, **823**, 102
 Ciardi, D. R., Beichman, C. A., Horch, E. P., & Howell, S. B. 2015, *ApJ*, **805**, 16
 Claytor, Z. R., van Saders, J. L., Santos, Â R. G., et al. 2020, *ApJ*, **888**, 43
 Collins, K. A., Kielkopf, J. F., Stassun, K. G., & Hessman, F. V. 2017, *AJ*, **153**, 77
 Dai, F., Masuda, K., & Winn, J. N. 2018, *ApJL*, **864**, L38
 Dai, F., Masuda, K., Winn, J. N., & Zeng, L. 2019, *ApJ*, **883**, 79
 Dai, F., Winn, J. N., Gandolfi, D., et al. 2017, *AJ*, **154**, 226
 Dalba, P. A., Gupta, A. F., Rodriguez, J. E., et al. 2020, *AJ*, **159**, 241
 Dawson, R. I., Johnson, J. A., Morton, T. D., et al. 2012, *ApJ*, **761**, 163
 De Silva, G. M., Freeman, K. C., Bland-Hawthorn, J., et al. 2015, *MNRAS*, **449**, 2604
 Deck, K. M., Holman, M. J., Agol, E., et al. 2013, *ApJL*, **774**, L15
 Demory, B.-O., Gillon, M., de Wit, J., et al. 2016, *Natur*, **532**, 207
 Demory, B.-O., Gillon, M., Seager, S., et al. 2012, *ApJL*, **751**, L28
 Dumusque, X., Bonomo, A. S., Haywood, R. D., et al. 2014, *ApJ*, **789**, 154
 Dupuy, T. J., Kratter, K. M., Kraus, A. L., et al. 2016, *ApJ*, **817**, 80
 Foreman-Mackey, D., Hogg, D. W., Lang, D., & Goodman, J. 2013, *PASP*, **125**, 306
 Fressin, F., Torres, G., Charbonneau, D., et al. 2013, *ApJ*, **766**, 81
 Fuhrmann, K. 1998, *A&A*, **338**, 161
 Fulton, B. J., Petigura, E. A., Blunt, S., & Sinukoff, E. 2018, *PASP*, **130**, 044504
 Furlan, E., Ciardi, D. R., Everett, M. E., et al. 2017, *AJ*, **153**, 71
 Gaia Collaboration, Brown, A. G. A., Vallenari, A., et al. 2016, *A&A*, **595**, A2
 Gaia Collaboration, Brown, A. G. A., Vallenari, A., et al. 2018, *A&A*, **616**, A1
 Gan, T., Shporer, A., Livingston, J. H., et al. 2020, *AJ*, **159**, 160
 Gilmore, G., & Reid, N. 1983, *MNRAS*, **202**, 1025
 Grunblatt, S. K., Howard, A. W., & Haywood, R. D. 2015, *ApJ*, **808**, 127
 Guo, X., Crossfield, I. J. M., Dragomir, D., et al. 2020, *AJ*, **159**, 239
 Hamer, J. H., & Schlafman, K. C. 2020, *AJ*, **160**, 138
 Hayward, T. L., Brandl, B., Pirger, B., et al. 2001, *PASP*, **113**, 105
 Haywood, R. D., Collier Cameron, A., Queloz, D., et al. 2014, *MNRAS*, **443**, 2517
 Hinkel, N. R., Timmes, F. X., Young, P. A., Pagano, M. D., & Turnbull, M. C. 2014, *AJ*, **148**, 54
 Hodapp, K. W., Jensen, J. B., Irwin, E. M., et al. 2003, *PASP*, **115**, 1388
 Howard, A. W., & Fulton, B. J. 2016, *PASP*, **128**, 114401
 Howard, A. W., Johnson, J. A., Marcy, G. W., et al. 2010, *ApJ*, **721**, 1467
 Howard, A. W., Marcy, G. W., Bryson, S. T., et al. 2012, *ApJS*, **201**, 15
 Howell, S. B., Everett, M. E., Sherry, W., Horch, E., & Ciardi, D. R. 2011, *AJ*, **142**, 19
 Huber, D., Zinn, J., Bojsen-Hansen, M., et al. 2017, *ApJ*, **844**, 102
 Isaacson, H., & Fischer, D. 2010, *ApJ*, **725**, 875
 Jenkins, J. M., Twicken, J. D., McCaulliff, S., et al. 2016, *Proc. SPIE*, **9913**, 99133E
 Jensen, E. 2013, Tapir: A Web Interface for Transit/eclipse Observability, Astrophysics Source Code Library, ascl:1306.007
 Kempton, E. M. R., Bean, J. L., Louie, D. R., et al. 2018, *PASP*, **130**, 114401
 Kipping, D. M. 2013, *MNRAS*, **435**, 2152
 Kreidberg, L. 2015, *PASP*, **127**, 1161
 Kreidberg, L., Koll, D. D. B., Morley, C., et al. 2019, *Natur*, **573**, 87
 Lacedelli, G., Malavolta, L., Borsato, L., et al. 2020, *MNRAS*, in press
 Li, G., Dai, F., & Becker, J. 2020, *ApJL*, **890**, L31
 Li, J., Tenenbaum, P., Twicken, J. D., et al. 2019, *PASP*, **131**, 024506
 Lightkurve Collaboration, Cardoso, J. V. d. M., Hedges, C., et al. 2018, Lightkurve: Kepler and TESS Time Series Analysis in Python, Astrophysics Source Code Library, ascl:1812.013
 Lindegren, L., Hernández, J., Bombrun, A., et al. 2018, *A&A*, **616**, A2
 Lithwick, Y., Xie, J., & Wu, Y. 2012, *ApJ*, **761**, 122
 Lopez, E. D. 2017, *MNRAS*, **472**, 245
 Lopez, E. D., & Fortney, J. J. 2014, *ApJ*, **792**, 1
 Marcus, R. A., Sasselov, D., Hernquist, L., & Stewart, S. T. 2010, *ApJL*, **712**, L73
 Marcy, G. W., & Butler, R. P. 1992, *PASP*, **104**, 270
 McCormac, J., Pollacco, D., Skillen, I., et al. 2013, *PASP*, **125**, 548
 McCully, C., Volgenau, N. H., Harbeck, D.-R., et al. 2018, *Proc. SPIE*, **10707**, 107070K
 Mills, S. M., Howard, A. W., Petigura, E. A., et al. 2019, *AJ*, **157**, 198
 Narita, N., Fukui, A., Kusakabe, N., et al. 2019, *JATIS*, **5**, 015001
 Parviainen, H., Palle, E., Zapatero-Osorio, M. R., et al. 2020, *A&A*, **633**, A28
 Petigura, E. A. 2015, PhD thesis, Univ. California
 Petigura, E. A., Howard, A. W., & Marcy, G. W. 2013, *PNAS*, **110**, 19273
 Petrovich, C., Deibert, E., & Wu, Y. 2019, *AJ*, **157**, 180

- Piskunov, N., & Valenti, J. A. 2017, *A&A*, **597**, A16
- Powell, M. J. D. 1964, *CompJ*, **7**, 155
- Pu, B., & Lai, D. 2019, *MNRAS*, **488**, 3568
- Rajpaul, V., Buchhave, L. A., & Aigrain, S. 2017, *MNRAS*, **471**, L125
- Rappaport, S., Sanchis-Ojeda, R., Rogers, L. A., Levine, A., & Winn, J. N. 2013, *ApJL*, **773**, L15
- Ricker, G. R., Winn, J. N., Vanderspek, R., et al. 2015, *JATIS*, **1**, 014003
- Rodriguez, D. 2016, Dr-Rodriguez/Kinematics-App: Stellar Kinematics V1.0, v1.0, Zenodo, doi:10.5281/zenodo.192159
- Rogers, L. A. 2015, *ApJ*, **801**, 41
- Salaris, M., Chieffi, A., & Straniero, O. 1993, *ApJ*, **414**, 580
- Sanchis-Ojeda, R., Rappaport, S., Winn, J. N., et al. 2014, *ApJ*, **787**, 47
- Sanchis-Ojeda, R., Winn, J. N., Dai, F., et al. 2015, *ApJL*, **812**, L11
- Savitzky, A., & Golay, M. J. E. 1964, *AnaCh*, **36**, 1627
- Schönrich, R., & Binney, J. 2009a, *MNRAS*, **399**, 1145
- Schönrich, R., & Binney, J. 2009b, *MNRAS*, **396**, 203
- Sharma, S., Stello, D., Buder, S., et al. 2018, *MNRAS*, **473**, 2004
- Silva Aguirre, V., Bojsen-Hansen, M., Slumstrup, D., et al. 2018, *MNRAS*, **475**, 5487
- Smith, A. M. S., Eigtmüller, P., Gurumoorthy, R., et al. 2020, *AN*, **341**, 273
- Smith, J. C., Stumpe, M. C., Van Cleve, J. E., et al. 2012, *PASP*, **124**, 1000
- Stassun, K. G., Collins, K. A., & Gaudi, B. S. 2017, *AJ*, **153**, 136
- Stassun, K. G., Oelkers, R. J., Pepper, J., et al. 2018, *AJ*, **156**, 102
- Stassun, K. G., & Torres, G. 2018, *ApJ*, **862**, 61
- Stumpe, M. C., Smith, J. C., Catanzarite, J. H., et al. 2014, *PASP*, **126**, 100
- Stumpe, M. C., Smith, J. C., Van Cleve, J. E., et al. 2012, *PASP*, **124**, 985
- Tamayo, D., Cranmer, M., Hadden, S., et al. 2020, *PNAS*, **117**, 18194
- Tayar, J., Claytor, Z. R., Huber, D., & van Saders, J. 2021, arXiv:2012.07957
- Ting, Y.-S., Conroy, C., Rix, H.-W., & Asplund, M. 2018, *ApJ*, **860**, 159
- Tokovinin, A., Mason, B. D., Hartkopf, W. I., Mendez, R. A., & Horch, E. P. 2018, *AJ*, **155**, 235
- Twicken, J. D., Catanzarite, J. H., Clarke, B. D., et al. 2018, *PASP*, **130**, 064502
- Valenti, J. A., & Piskunov, N. 1996, *A&AS*, **118**, 595
- Van Eylen, V., Albrecht, S., Huang, X., et al. 2019, *AJ*, **157**, 61
- van Saders, J. L., Ceillier, T., Metcalfe, T. S., et al. 2016, *Natur*, **529**, 181
- van Saders, J. L., & Pinsonneault, M. H. 2013, *ApJ*, **776**, 67
- Weiss, L. M., & Marcy, G. W. 2014, *ApJL*, **783**, L6
- Weiss, L. M., Marcy, G. W., Petigura, E. A., et al. 2018, *AJ*, **155**, 48
- Weiss, L. M., Rogers, L. A., Isaacson, H. T., et al. 2016, *ApJ*, **819**, 83
- Wheatley, P. J., West, R. G., Goad, M. R., et al. 2018, *MNRAS*, **475**, 4476
- Yee, S. W., Petigura, E. A., & von Braun, K. 2017, *ApJ*, **836**, 77
- Zeng, L., Jacobsen, S. B., Sasselov, D. D., et al. 2019, *PNAS*, **116**, 9723
- Ziegler, C., Tokovinin, A., Briceño, C., et al. 2020, *AJ*, **159**, 19